

A Volume Limited Survey of mCP Stars Within 100pc II: Rotational and Magnetic Properties

J. Sikora,^{1,2} G. A. Wade,² J. Power,^{1,2,4} C. Neiner³

¹*Department of Physics, Engineering Physics & Astronomy, Queen's University, Kingston, ON Canada, K7L 3N6*

²*Department of Physics and Space Science, Royal Military College of Canada, PO Box 17000 Kingston, Ontario K7K 7B4, Canada*

³*LESIA, Observatoire de Paris, PSL University, CNRS, Sorbonne Universit, Univ. Paris Diderot, Sorbonne Paris Cit,
5 place Jules Janssen, 92195 Meudon, France*

⁴*Large Binocular Telescope Observatory, 933 North Cherry Avenue, Tucson, AZ 85721, USA*

Accepted 2018 Oct. 23

ABSTRACT

Various surveys focusing on the magnetic properties of intermediate-mass main sequence (MS) stars have been previously carried out. One particularly puzzling outcome of these surveys is the identification of a dichotomy between the strong ($\gtrsim 100$ G), organized fields hosted by magnetic chemically peculiar (mCP) stars and the ultra-weak ($\lesssim 1$ G) fields associated with a small number of non-mCP MS stars. Despite attempts to detect intermediate strength fields (i.e. those with strengths $\gtrsim 10$ G and $\lesssim 100$ G), remarkably few examples have been found. Whether this so-called “magnetic desert”, separating the stars hosting ultra-weak fields from the mCP stars truly exists has not been definitively answered. In 2007, a volume-limited spectropolarimetric survey of mCP stars using the MuSiCoS spectropolarimeter was initiated to test the existence of the magnetic desert by attempting to reduce the biases inherent in previous surveys. Since then, we have obtained a large number of ESPaDOnS and NARVAL Stokes V measurements allowing this survey to be completed. Here we present the results of our homogeneous analysis of the rotational periods (inferred from photometric and magnetic variability) and magnetic properties (dipole field strengths and obliquity angles) of the 52 confirmed mCP stars located within a heliocentric distance of 100 pc. No mCP stars exhibiting field strengths $\lesssim 300$ G are found within the sample, which is consistent with the notion that the magnetic desert is a real property and not the result of an observational bias. Additionally, we find evidence of magnetic field decay, which confirms the results of previous studies.

Key words: Stars: early-type, Stars: chemically peculiar, Stars:rotation, Stars:magnetic

1 INTRODUCTION

The generation and broader characteristics of magnetic fields of cool stars are reasonably well understood within the framework of stellar dynamo theory (e.g. Charbonneau 2010). In contrast, the origin of the magnetic fields of main sequence (MS) stars more massive than about $1.5 M_{\odot}$ remains a profound mystery. Over the past several decades, many clues related to this problem have been reported.

It is now reasonably well established that all magnetic, chemically peculiar stars (i.e. Ap/Bp stars, hereinafter referred to as mCP stars) host organized magnetic fields with strengths as large as 30 kG (e.g. Landstreet 1982; Shorlin et al. 2002). In general, the large-scale structures of these fields are relatively simple (e.g. Babcock 1956; Kochukhov et al. 2015), although a few obvious examples of more complex fields have been discovered (e.g. Kochukhov et al.

2011; Silvester et al. 2017). Furthermore, both young and evolved MS mCP stars are known to exist (e.g. Wade 1997; Kochukhov & Bagnulo 2006), which suggests that these fields are stable over long time periods. Surface magnetic fields have been detected on some Herbig Ae/Be stars (e.g. Wade et al. 2007; Alecian et al. 2013), which are likely the progenitors of the MS mCP stars. All of these findings are consistent with the notion that the fields hosted by mCP stars are fossil remnants left over from an earlier stage in the star’s evolution (the *fossil field* theory, Cowling 1945; Moss 1984; Landstreet 1987).

One property of stellar magnetism of upper MS stars that is not currently well explained by the fossil field theory is the fact that only ~ 10 per cent of all MS A- and B-type stars (e.g. Wolff 1968; Smith 1971) host strong, organized surface magnetic fields. Shorlin et al. (2002), Bag-

nulo et al. (2006), and Aurière et al. (2010) obtained a large number of magnetic measurements of non-mCP MS stars of spectral types A and B with median uncertainties of 20 G, 95 G, and 2 G, respectively, however, no magnetic detections were reported. Makaganiuk et al. (2010) carried out a similar survey of HgMn stars – obtaining typical longitudinal field uncertainties ~ 10 G and as low as 0.8 G – but did not report any detections of circularly polarized Zeeman signatures. Recently, fields with strengths $\lesssim 1$ G (so-called ultra-weak, or Vega-type, fields) were detected on a small number of non-mCP stars (e.g. Lignières et al. 2009; Petit et al. 2011; Blazère, Neiner & Petit 2016). Based on these findings, Petit et al. (2011) speculate that a much higher fraction of MS A-type stars (i.e. $\gg 10$ per cent) may host ultra-weak surface fields. Regardless, the dichotomy between the strongly magnetic and the non-magnetic (or very weakly magnetic) MS A-type stars is unlikely to be entirely explained by the sensitivity of the current generation of spectropolarimeters. In the case of Vega, it is reported that its ultra-weak field exhibits a highly complex field structure (Petit et al. 2010) that is atypical of the strongly magnetic mCP stars. It is therefore plausible that the ultra-weak fields are a distinct phenomenon, which may have an origin that differs from that of the strong, organized fields hosted by mCP stars (Braithwaite & Cantiello 2013).

In 2007, Aurière et al. (2007) explored the weak field regime of mCP stars by obtaining high-precision longitudinal field measurements of 28 such objects with reportedly weak or otherwise poorly constrained field strengths. All of the observed mCP stars were detected in their spectropolarimetric observations, and were inferred to exhibit dipolar field strengths of $B_d \gtrsim 100$ G with the two weakest fields found to have $B_d = 100^{+392}_{-100}$ G and $B_d = 229^{+248}_{-76}$ G. Aurière et al. (2007) hypothesized that there exists a critical field strength ($B_c \approx 300$ G), which corresponds to the minimum field strength that an mCP star must host in order to be invulnerable to a magnetohydrodynamic pinch-instability (Tayler 1973; Spruit 2002). In this scenario, every intermediate-mass MS star may be initially “assigned” a field strength (perhaps based on external factors, e.g. the local field properties at its location of formation, the presence of a companion, etc.) drawn from a probability distribution that increases towards lower field strengths; only those fields exceeding B_c are able to be maintained, which results naturally in the so-called “magnetic desert” (i.e. the dichotomy between the ultra-weak fields detected on a small number of non-mCP stars and the strong fields hosted by mCP stars, Lignières et al. 2014).

While the detection of ultra-weak fields may not directly contradict the existence of a critical lower field strength limit, two stars have been found reportedly hosting fields with intermediate strengths (i.e. $10 \lesssim B_d \lesssim 100$ G, which is lower than the typical $B_c \sim 300$ G proposed by Aurière et al. 2007). The massive early B-type star β CMa reportedly hosts a field with $B_d < 230$ G (Fossati et al. 2015) while the primary component of the spectroscopic binary HD 5550 is reportedly an Ap star hosting a field having $B_d < 85$ G (Alecian et al. 2016). We discuss these two examples in Sect. 7; however, we note that the fact that nearly all mCP stars are found hosting fields $\gtrsim 100$ G despite the current detection limits that have been achieved remains conspicuous.

A potential problem with many of the reported empir-

ical properties of mCP stars – including the existence of the magnetic desert – is the fact that they are generally inferred from intrinsically biased surveys: they are either biased towards brighter objects (magnitude limited surveys) or those hosting stronger, more easily detectable fields (field-strength limited surveys). In 2007, a volume-limited survey of mCP stars located within a heliocentric distance of 100 pc was initiated by Power (2007) in order to reduce these observational biases. This work yielded the magnetic properties of a large number of mCP stars in the sample using measurements obtained with the now-decommissioned MuSiCoS spectropolarimeter at the Pic du Midi Observatory. However, at the completion of that investigation, nearly half of the sample remained either unobserved or had relatively poor constraints on their field strengths and geometries. We have recently completed this survey using measurements obtained by ESPaDOnS and NARVAL.

In Paper I, we described in detail the sample of mCP and non-mCP stars included in the volume-limited sample. This sample was compiled using Hipparcos parallaxes (ESA 1997) to identify all MS stars with masses $\geq 1.4 M_\odot$ (i.e. all early-F, A-, and B-type MS stars) located within the adopted distance limit of 100 pc. We then cross-referenced this list with the Catalogue of Ap, HgMn and Am stars (Renson, Gerbaldi & Catalano 1991; Renson & Manfroid 2009) as well as the Spectral Classifications compiled by Skiff (2014) in order to identify confirmed and candidate mCP stars. Ultimately, 52 confirmed mCP stars were identified based on published, archived, and newly obtained photometric, spectroscopic, and spectropolarimetric (i.e. Stokes V) measurements. We derived fundamental parameters (effective temperatures, luminosities, masses, ages, etc.) of all of the intermediate-mass MS stars in the sample. Average surface chemical abundances of the mCP stars were also derived. The analysis presented in Paper I serves as a starting point for the magnetic analysis presented here. The results included in this second paper (i.e. Paper II) are organized as follows.

In Sect. 2, we discuss the newly obtained or previously unpublished MuSiCoS, ESPaDOnS, and NARVAL Stokes V observations. In Sect. 3, we present our analysis of these measurements and how they are used to derive longitudinal magnetic field measurements; the measurements are then used to help identify each star’s rotational period, as discussed in Sect. 4. In Sect. 5, we derive the magnetic field strengths and geometries and in Sect. 6, we search for evolutionary changes of the field strengths. Finally, in Sect. 7 we discuss the results while presenting our conclusions drawn from the survey.

2 NEW OBSERVATIONS

2.1 MuSiCoS spectropolarimetry

The MuSiCoS échelle spectropolarimeter was installed on the 2 m Télescope Bernard Lyot (TBL) at the Pic du Midi Observatory in 1996 where it was operational until its decommissioning in 2006. It had a resolving power ~ 35000 and was capable of obtaining circularly polarized (Stokes V) spectra from 3900 to 8700 Å (Donati et al. 1999). For this study, we used a total of 151 Stokes V observations of

23 stars that were obtained from Feb. 12, 1998 to June 8, 2006. These observations were reduced using the ESPRIT software package (Donati et al. 1997).

We note that the raw MuSiCoS spectra used in this study are unavailable and we have relied on normalized and reduced spectra from a private archive. All of the available spectra span a wavelength range of 4 500 to 6 600 Å rather than the full range presumably associated with the raw spectra. Furthermore, an automatic normalization routine built into the ESPRIT reduction package had been applied to the spectra.

2.2 ESPaDOnS & NARVAL spectropolarimetry

The ESPaDOnS and NARVAL échelle spectropolarimeters are twin instruments installed at the Canada-France-Hawaii Telescope (CFHT), and TBL, respectively. They have a resolving power $\sim 65\,000$ and are optimized for a wavelength range of approximately 3 600 Å to 10 000 Å.

We obtained 95 Stokes V observations of 37 stars from Aug. 2, 2015 to Aug. 10, 2016 using ESPaDOnS. Twenty-three Stokes V observations of 3 stars were obtained using NARVAL from Aug. 20, 2016 to Feb. 20, 2017. All of the observations obtained using ESPaDOnS and NARVAL were reduced with the LIBRE-ESPRIT software package, which is an updated version of the ESPRIT reduction package that was applied to the MuSiCoS data (Donati et al. 1997).

3 MAGNETIC MEASUREMENTS

Organized magnetic fields that are present in the photospheres of mCP stars may be detected by identifying Zeeman signatures in Stokes V spectropolarimetric observations. While these signatures are typically weak in individual spectral lines, the SNRs can be significantly increased by calculating Least-Squares Deconvolution (LSD) profiles (Donati et al. 1997; Kochukhov, Makaganiuk & Piskunov 2010). This cross-correlation technique involves essentially averaging a large number of spectral lines (typically $\gtrsim 100$) having similarly-shaped profiles. It has been widely used in the study of mCP star magnetism (e.g. Wade et al. 2000; Shorlin et al. 2002).

3.1 Confirmed mCP Stars

We generated LSD profiles for all of the available Stokes V observations. This was carried out by first generating line lists containing wavelengths, depths, and Landé factors, from the Vienna Atomic Line Database (VALD) (Ryabchikova et al. 2015). Custom lists specific to each star in the sample were obtained using Extract Stellar requests specifying the effective temperatures (T_{eff}), surface gravities ($\log g$), and chemical abundances derived in Paper I (solar abundances were adopted for those elements without estimated abundances); a microturbulence value (v_{mic}) of 0 km s^{-1} was used along with a detection threshold of 0.05 and a wavelength range of 4 000 to 7 000 Å. Line masks were subsequently generated from each of the line lists and compared with the observed spectra: any lines in the line mask that were found to overlap with either telluric lines or broad Balmer lines were removed. The Stokes V , Stokes I ,

and diagnostic null (i.e. the flux obtained by combining the subexposures such that the net polarization of the source is cancelled, Eqn. 3 of Donati et al. 1997) measurements associated with each spectropolarimetric observation were normalized by fitting a multi-order polynomial to the continuum flux of each spectral order. An example of an LSD profile calculated using one of the observed spectra and its associated line mask is shown in Fig. 1. Additional examples are shown in the electronic version of this paper.

The Stokes I/I_c and V/I_c LSD profiles were used to measure the disk-averaged longitudinal magnetic field ($\langle B_z \rangle$) as given by equation 1 of Wade et al. (2000). We used mean wavelengths (λ_{avg}) and mean Landé factors (z_{avg}) calculated from the customized line masks associated with each star. Prior to each $\langle B_z \rangle$ measurement, the Stokes I/I_c and V/I_c LSD profiles were renormalized by fitting a 1st order polynomial (i.e. a linear function) to the regions where $I/I_c \sim 1$ and $V/I_c \sim 0$ (typically at $v \approx \pm 100\text{ km s}^{-1}$). Any radial velocity shift that was apparent in the Stokes I/I_c LSD profile, as inferred from the calculation of the profile’s “center of gravity” (i.e. the integral of vI/I_c over that of I/I_c), was removed. The v integration limits were chosen to encompass the absorption profile as determined by eye. The derived values of $\langle B_z \rangle$ associated with the confirmed mCP stars are listed in Table 1.

In addition to the previously unpublished $\langle B_z \rangle$ measurements listed in Table 1, we also derived $\langle B_z \rangle$ from archived ESPaDOnS and NARVAL Stokes V observations. In these cases, we applied the same analysis that was used with the new observations reported in this study. This ensured that both the new and archived observations yielded consistent $\langle B_z \rangle$ measurements such that any apparent variability cannot be attributed to the use of different line masks (i.e. all $\langle B_z \rangle$ values are obtained using the same measurement system). In total, we used 400 measurements of 42 confirmed mCP stars derived using the line masks generated in this study – corresponding to a median value of six observations per star. These $\langle B_z \rangle$ measurements exhibit a median uncertainty of $\sigma_{\langle B_z \rangle} = 18\text{ G}$. Published $\langle B_z \rangle$ measurements exist for the majority of the confirmed mCP stars. We compiled and included many of these measurements in our analysis when no corresponding archival Stokes V observations were found. For ten out of the fifty-two confirmed mCP stars, only previously published measurements were available (i.e. no new or archived Stokes V observations were available). Note that these published data are not derived using the same measurement system as used for the $\langle B_z \rangle$ measurements that we derived from the Stokes V observations and analyzed herein.

In summary, a total of 947 new, archived, and published $\langle B_z \rangle$ measurements of the confirmed mCP stars were used in this study, corresponding to a median number of observations per star of 17. The measurements exhibit a median $\sigma_{\langle B_z \rangle}$ of 49 G and a median minimum $\sigma_{\langle B_z \rangle}$ per star of 15 G. For four of the fifty-two stars, fewer than five observations are available. Two detections of HD 117025 are reported by Kochukhov & Bagnulo (2006) while, due to its relatively low declination of -45° , we were only able to obtain a single observation of HD 217522. For HD 29305, only four archived HARPSpol Stokes V observations are available while for HD 56022, we obtained four new Stokes V observations using ESPaDOnS.

Table 1. Observations of confirmed mCP stars – those stars for which at least one definite detection was obtained based on the criterion proposed by Donati et al. (1997). Columns 1 to 5 contain the HD number, instrument used to obtain the observation (ESP = ESPaDOnS, MUS = MuSiCoS, and NAR = NARVAL), HJD, rotational phase, and the derived $\langle B_z \rangle$ value and its associated uncertainty. The full table will appear only in the electronic version of the paper.

HD	Inst.	HJD	Phase	$\langle B_z \rangle$ (G)	HD	Inst.	HJD	Phase	$\langle B_z \rangle$ (G)
15089	MUS	3040.343	0.259	223 ± 93	72968	ESP	7443.892	0.434	-81 ± 36
	MUS	3586.543	0.077	450 ± 23		ESP	7447.848	0.739	86 ± 26
	MUS	3589.652	0.864	506 ± 18		MUS	3748.583	0.774	346.4 ± 8.4
	MUS	3590.561	0.386	-258 ± 20		MUS	3749.549	0.945	343.0 ± 7.3
	MUS	3591.597	0.981	509 ± 19		MUS	3755.429	0.985	307 ± 16
	MUS	3594.551	0.678	-166 ± 24		MUS	3756.527	0.179	323.5 ± 7.0
	MUS	3607.557	0.150	441 ± 32		ESP	7416.994	0.763	334.1 ± 5.2
	MUS	3616.513	0.296	11 ± 24		ESP	7498.720	0.221	335.2 ± 3.8
15144	MUS	2253.385	0.716	-568 ± 13	74067	ESP	7500.781	0.586	266.8 ± 2.5
	MUS	2254.408	0.057	-619 ± 12		ESP	7330.146	0.046	1024 ± 11
	MUS	3410.324	0.620	-567 ± 18		ESP	7331.099	0.352	-147 ± 10
	MUS	3613.503	0.392	-551 ± 15		ESP	7348.156	0.828	748 ± 38
	MUS	3615.559	0.078	-612 ± 10		ESP	7415.993	0.605	-303 ± 12
	MUS	3617.570	0.749	-586 ± 11		ESP	7440.875	0.592	-370 ± 34
18296	ESP	7556.127	0.190	91 ± 19	96616	ESP	7445.857	0.192	562 ± 26
	ESP	7561.124	0.923	169 ± 19		ESP	7446.838	0.506	-480 ± 28
	ESP	7610.142	0.918	195.7 ± 9.7		ESP	7358.169	0.668	-58 ± 15
24712	MUS	857.333	0.180	765 ± 13		ESP	7441.990	0.172	213 ± 16
	MUS	1924.360	0.830	763 ± 12		ESP	7444.970	0.399	-153 ± 22
	MUS	3247.675	0.052	1033 ± 17		ESP	7447.937	0.620	-101 ± 13
56022	ESP	7325.149	0.210	139 ± 32		ESP	7448.964	0.043	325 ± 14
	ESP	7438.845	0.941	195 ± 24					

Table 2. Spectropolarimetric observations of those stars for which no Zeeman signatures were detected. Columns 1 to 6 contain the HD number, instrument used to obtain the observation (ESP = ESPaDOnS, MUS = MuSiCoS, NAR = NARVAL), HJD, exposure time, number of consecutive observations, and the derived $\langle B_z \rangle$ value and its associated uncertainty.

HD	Inst.	HJD +2 450 000	t_{exp} (s)	#	$\langle B_z \rangle$ (G)	HD	Inst.	HJD +2 450 000	t_{exp} (s)	#	$\langle B_z \rangle$ (G)
358	ESP	7561.129	15	1	31 ± 19		MUS	3747.683	3200	1	180 ± 180
4853	ESP	7239.132	200	1	24 ± 19		MUS	3750.683	3200	1	70 ± 180
27411	ESP	7435.763	8	1	0 ± 11		MUS	3755.683	3200	1	210 ± 160
27749	ESP	7435.766	5	1	5.4 ± 9.5		MUS	3756.626	3200	1	80 ± 140
67523	ESP	7414.991	5	1	0.5 ± 1.9		MUS	3864.422	2400	1	50 ± 220
78362	MUS	858.604	1200	1	-0.2 ± 3.9		MUS	3874.440	2400	1	-90 ± 180
	MUS	1202.554	1635	1	-8 ± 25		MUS	3885.401	2400	1	120 ± 240
	ESP	7412.001	5	1	-6.3 ± 5.7		MUS	3892.366	2400	1	-20 ± 190
90763	ESP	7325.137	8	1	34 ± 54		ESP	7236.789	330	2	39 ± 26
	ESP	7327.160	8	1	79 ± 47		ESP	7261.749	330	2	-47 ± 28
	ESP	7328.157	8	1	-18 ± 50		ESP	7262.733	330	2	10 ± 25
	ESP	7329.106	8	1	60 ± 53		ESP	7265.730	330	2	3 ± 43
	ESP	7330.122	31	1	6 ± 27	120025	ESP	7414.075	123	1	-4.6 ± 8.2
	ESP	7522.802	60	1	12 ± 23	125335	ESP	7408.155	200	1	-4.0 ± 3.2
102942	ESP	7412.006	37	1	-8 ± 10	136729	NAR	7800.669	3188	1	15 ± 68
	ESP	7497.913	37	1	0 ± 10	139478	NAR	7801.609	1176	1	-2.9 ± 7.6
	ESP	7498.878	200	2	-4.3 ± 3.2	149748	ESP	7409.126	225	1	20 ± 13
	ESP	7500.885	200	2	-4.0 ± 3.2	156164	ESP	7560.979	40	1	190 ± 290
105702	ESP	7409.107	6	1	22 ± 17	189849	ESP	7476.130	19	1	3.8 ± 3.6
	ESP	7495.949	6	2	11 ± 16	202627	ESP	7261.984	217	2	14 ± 16
	ESP	7497.923	6	1	-16 ± 11	206742	ESP	7262.001	50	1	-9 ± 26
	ESP	7498.955	6	1	13 ± 13		ESP	7262.001	50	1	71 ± 63
	ESP	7500.902	6	1	-15 ± 11	221675	ESP	7554.124	100	1	-3 ± 13
115735	MUS	1600.662	2595	1	-100 ± 190						

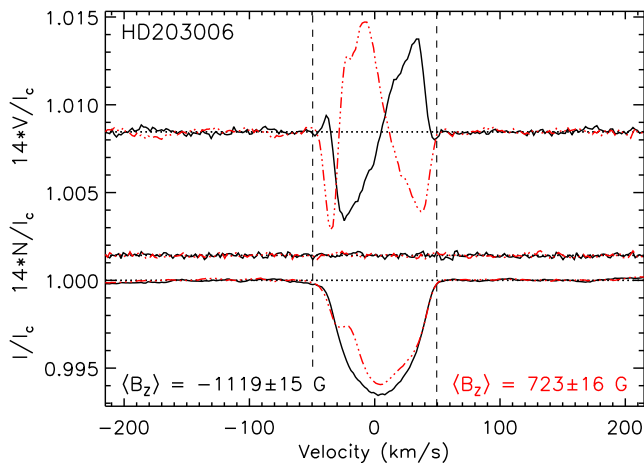


Figure 1. Two examples of the Stokes V (top), diagnostic null (middle), and Stokes I (bottom) LSD profiles derived from the spectropolarimetric observations obtained using ESPaDOnS. The vertical dashed lines indicate the adopted integration limits used to derive the displayed $\langle B_z \rangle$ values. Note that the Stokes V and diagnostic null profiles have been scaled by a factor of 14. Additional examples are included in the electronic version of this paper.

3.2 Null Results

As discussed in Paper I, during the initial phase of this study, we identified a number of stars within the Catalogue of Ap, HgMn and Am stars (Renson & Manfroid 2009) reported as being potential mCP members. Additionally, several Am and HgMn stars were found to exhibit Δa , $\Delta(V_1 - G)$, or ΔZ photometric indices consistent with those exhibited by mCP stars (e.g. Maitzen, Pressberger & Paunzen 1998; Bayer et al. 2000; Paunzen & Maitzen 2005). We obtained Stokes V observations for 19 of these stars using MuSiCoS, ESPaDOnS, and NARVAL in order to search for Zeeman signatures. The observations were analyzed using the same LSD technique that was applied to the confirmed mCP stars; however, the line masks generated from the VALD line lists used a surface gravity of $\log g = 4.0$ (cgs) and a solar metallicity (individual chemical abundances were not specified).

No Zeeman signatures were detected from the observations of the 19 stars. The minimum $\langle B_z \rangle$ uncertainties obtained for each star ranged from 1.9 G to 69 G with a median value of 11.4 G. Kochukhov & Bagnulo (2006) report a measured $\langle B_z \rangle = -56 \pm 68$ G for one of the 19 stars, HD 202627; we obtained a single observation of this star, which yielded a lower uncertainty and no detection ($\langle B_z \rangle = 14 \pm 17$ G). The observations are summarized in Table 2 where we list the measured longitudinal field values.

4 ROTATIONAL PERIODS AND INCLINATION ANGLES

Magnetic CP stars are well known to be associated with the periodic variability of surface-averaged longitudinal magnetic field measurements (e.g. Pyper 1969; Borra, Landstreet & Mestel 1982; Bohlender, Landstreet & Thompson 1993). The Oblique Rotator Model (ORM) attributes these variations to a product of (1) the star’s rotation and

(2) the presence of a stable surface magnetic field that is non-axisymmetric with respect to the star’s rotational axis (Stibbs 1950; Preston 1967). A similar explanation for the long-period ($\gtrsim 1$ d) photometric variability that is commonly associated with these stars is also widely accepted: the variations are understood to be produced by the presence of inhomogeneous structures (i.e. chemical abundance spots) located within the rotating star’s atmosphere (e.g. Wolff 1969; Adelman, Dukes, Jr. & Pyper 1992; Krtićka et al. 2015). Therefore, the characterization of both the rotationally modulated $\langle B_z \rangle$ and photometric measurements may allow for an mCP star’s rotational period (P_{rot}) to be constrained.

Rotational periods of the majority of the confirmed mCP stars in our sample have been previously published (e.g. Catalano, Leone & Kroll 1998; Renson & Catalano 2001). We performed a period search analysis (described below) on all of the $\langle B_z \rangle$ data sets, which consist of published $\langle B_z \rangle$ measurements along with those measurements derived from either new or re-analyzed archival Stokes V spectra, as discussed in Sect. 3.1. The analysis typically yielded a number of plausible rotational periods, which were then compared with those that have been previously reported in the literature. The same period search analysis was also carried out on Hipparcos Epoch Photometry (H_p) (ESA 1997), which aided in the correct identification of P_{rot} . For each of the 52 mCP stars, between 42 and 260 H_p measurements are available spanning 3 yrs. The minimum and average time intervals between each measurement are approximately 21 min and 11 d, respectively. Each measurement has been assigned a quality flag, which indicates potential problems (e.g. high background flux or inconsistent values obtained by the NDAC and FAST data reductions). Any measurements exhibiting quality flag numbers (referred to as ‘transit flags’ in the Hipparcos catalogue) > 20 were identified but not removed from the analysis. This decision to retain flagged measurements was based on the fact that, in certain cases, all of the star’s measurements exhibited transit flags > 20 despite the detection of variability that was consistent with that of the $\langle B_z \rangle$ measurements. For most of the stars having flagged measurements, the number of flagged measurements was relatively insignificant and did not strongly influence the period search analysis.

Both the $\langle B_z \rangle$ measurements and the Hipparcos Epoch Photometry were analyzed using two methods to identify the most probable rotational periods. First, normalized Lomb-Scargle periodograms were generated using an IDL routine based on the algorithm presented by Press (2007). This method yields the spectral power distribution, which is used to identify statistically significant frequencies (i.e. those having false alarm probabilities < 3 per cent) inherent to an unevenly sampled time series data set. A substantial benefit of this method is that it can be performed relatively quickly compared to the second period search analysis described below thereby allowing potentially relevant periods to be recognized efficiently. However, for the majority of the mCP stars, an insufficient number of $\langle B_z \rangle$ measurements were available to yield statistically significant frequencies. This technique was found to be more useful when applied to the Hipparcos Epoch Photometry because of the larger number of data points available for each star. The $\langle B_z \rangle$ measurements were then used to verify that the derived Hippar-

cos period provided an acceptable phasing of the magnetic data.

The periodogram calculation was followed by the application of a commonly used period search analysis described, for example, by Alecian et al. (2014). The method involves fitting the time series data to a function consisting of the first two or three terms in a Fourier series using a range of fixed periods (P); plausible rotational periods are identified as those which yield the lowest χ^2 values. We adopted a 2nd order sinusoidal fitting function given by

$$f(t) = C_0 + C_1 \sin(2\pi[t - t_0]/P + \phi_1) + C_2 \sin(4\pi[t - t_0]/P + \phi_2) \quad (1)$$

where t_0 is the epoch (set to zero during the period search analysis) and C_0 , C_1 , C_2 , ϕ_1 , and ϕ_2 are free parameters. We defined an initial grid of period values having a step size of $\Delta P = 10^{-4}$ d and spanning $0.1 \leq P \leq 25$ d. For each P value in the grid, the best fit was derived and the associated χ^2 values were recorded. This analysis was repeated with $C_2 \equiv 0$ (reducing Eqn. 1 to a 1st order sinusoidal fitting function), which was frequently found to decrease the number of statistically significant periods derived from the $\langle B_z \rangle$ data sets. This is related to the fact that longitudinal field measurements of mCP stars are most sensitive to the dipole component (e.g. Eqn. 68 of Bagnulo, Innocenti & Degl’Innocenti 1996). Nevertheless, significant higher-degree contributions to $\langle B_z \rangle$ curves are often detected in high-precision data (e.g. Kochukhov et al. 2004; Kochukhov, Makaganiuk & Piskunov 2010; Silvester, Kochukhov & Wade 2015).

Uncertainties in the adopted rotational periods ($\sigma_{P_{\text{rot}}}$) were estimated by calculating the 3σ confidence limits associated with the width of the χ^2 trough; if $\sigma_{P_{\text{rot}}} \leq \Delta P$, the grid’s range ($P_{\text{max}} - P_{\text{min}}$) and ΔP was reduced, the grid was re-centered on the relevant period, and the grid of χ^2 values was re-calculated. If the final $\sigma_{P_{\text{rot}}}$ was found to be appreciably less than the published $\sigma_{P_{\text{rot}}}$ – or if no $\sigma_{P_{\text{rot}}}$ was reported with the published P_{rot} – the new P_{rot} and $\sigma_{P_{\text{rot}}}$ was adopted.

After identifying P_{rot} and obtaining $\sigma_{P_{\text{rot}}}$, either through a period search analysis or from the literature, final 1st and 2nd order sinusoidal fits to each star’s $\langle B_z \rangle(t)$ and $H_p(t)$ measurements were derived (2nd order fits were only derived for those data sets consisting of more than 5 data points). The epoch of each star was defined such that $\langle B_z \rangle(t_0) = |C_0 + C_1|$ (i.e. the maximum, unsigned longitudinal field strength) while ϕ_1 and ϕ_2 were constrained such that $C_1 > 0$ and $C_2 > 0$. Note that the way in which the epoch is defined and the way in which C_1 and C_2 are constrained implies that, for the fits to $\langle B_z \rangle$, $\phi_1 = \pm\pi/2$ while ϕ_2 is a free parameter; for the fits to H_p , both ϕ_1 and ϕ_2 are unrestricted free parameters.

Published periods for 18/52 of the mCP stars were found to be in agreement with those associated with the minimal χ^2 value and/or maximal Lomb-Scargle spectral power yielded by our $\langle B_z \rangle$ and Hipparcos Epoch Photometry period search analyses. In these cases, the stars’ rotational period could be unambiguously identified. For 21/52 of the stars, the most probable periods inferred from the period search analysis were not consistent with the published periods. The rotational periods of these stars were determined by identifying those published periods, which are primar-

ily inferred from photometric variability, that are consistent with local χ^2 minima having values within 3σ confidence limits of the global χ^2 minima. We encountered complications regarding the identification of P_{rot} for the remaining 12/52 stars (discussed below in Sections 4.1 to 4.8); however, we note that in most of these cases, final rotational periods were adopted.

In total, we adopted rotational periods for 48/52 of the mCP stars in the sample. The phased $\langle B_z \rangle$ measurements and the associated best fitting sinusoidal functions are shown in Figures 3, 4, and 5. The corresponding phased H_p measurements are only included in the electronic version of this paper. The $\langle B_z \rangle$ measurements as a function of HJD of the 4 stars with > 1 measurement and for which we were unable to establish P_{rot} values are shown in Fig. 6.

In the following eight subsections (Sections 4.1 to 4.8), we discuss those stars for which P_{rot} could not be unambiguously determined due to (1) an insufficient number of measurements, (2) no detection of photometric or $\langle B_z \rangle$ variability, or (3) disagreement with published rotational periods.

4.1 HD 27309 and HD 72968

The most precise published $P_{\text{rot}} = 1.5688840(47)$ d (North & Adelman 1995) for HD 27309 was found to be consistent with the most probable period inferred from the Hipparcos photometry; however, both this period and its second harmonic exhibit poor agreement with the variability of the $\langle B_z \rangle$ measurements when fit to a 1st order sinusoidal function. A high quality 2nd order sinusoidal fit (Eqn. 1) is obtained using the published P_{rot} , which exhibits $C_1 \sim C_2$ (i.e. comparable amplitudes of the 1st and 2nd order terms). HD 72968 is similar in that Maitzen, Albrecht & Heck (1978) report a period of 11.305(2) d, however, this period is inconsistent with both the $\langle B_z \rangle$ and Hipparcos measurements. Furthermore, the $v \sin i$ value and stellar radius derived in Paper I imply a maximum P_{rot} of approximately 8.2 d. We find that halving the 11.305 d period ($P_{\text{rot}} = 5.6525$ d) yields acceptable 1st and 2nd order fits to the Hipparcos photometry and an acceptable 2nd order fit to $\langle B_z \rangle$. We note that Aurière et al. (2007) adopt the same 5.6525 d period. Both the adopted magnetically-inferred rotational periods for HD 27309 and HD 72968 should be verified using additional measurements.

4.2 HD 74067

No published rotational period could be found for HD 74067. We were able to derive P_{rot} for HD 74067 based on the identification of a single statistically significant period in the $\langle B_z \rangle$ χ^2 distribution, which was found to be consistent with a local χ^2 minima derived from the Hipparcos photometry.

4.3 HD 128898

As noted by Mathys & Hubrig (1997), the $\langle B_z \rangle$ measurements of HD 128898 obtained by Mathys (1991, 1994) and Mathys & Hubrig (1997) do not exhibit a trend that is consistent with the star’s known rotational period (4.4790 d, Kurtz et al. 1994). The authors attribute this to the low

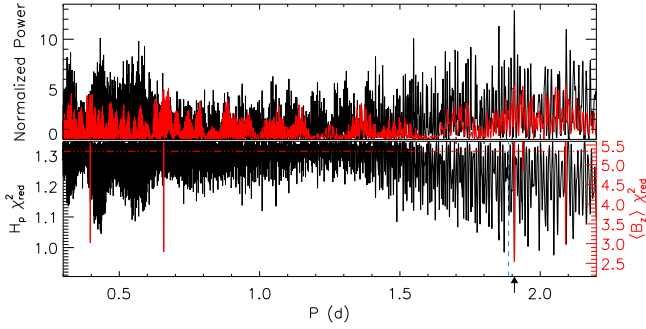


Figure 2. Normalized Lomb-Scargle periodograms (top) and χ^2 distributions derived using the 1st order sinusoidal function (bottom) associated with the Hipparcos (black) and $\langle B_z \rangle$ (red) measurements of HD 130559. The horizontal dot-dashed red line corresponds to the $\langle B_z \rangle$ 3 σ confidence limit calculated with respect to χ^2_{\min} ; the H_p periods shown in the χ^2 distribution exhibit confidence limits $< 0.1\sigma$. The black arrow indicates the adopted $P_{\text{rot}} = 1.90798(71)$ d. The vertical dashed blue line appearing in the χ^2 plot corresponds to the 1.8871(8) d period identified by Wraight et al. (2012) based on STEREO photometry, which is not consistent with the $\langle B_z \rangle$ measurements.

amplitude of $\langle B_z \rangle$ variability. We did not obtain nor find any new $\langle B_z \rangle$ measurements that could potentially better constrain the star’s magnetic properties.

4.4 HD 130559

Two possible rotational periods (1.8871(8) d and 25.4(2) d) of HD 130559 are reported by Wraight et al. (2012) based on the detection of strong photometric variability using the STEREO spacecraft. No statistically significant variability was detected from the Hipparcos photometry. Our analysis includes 12 $\langle B_z \rangle$ measurements obtained with MuSiCoS; the period search analysis of this data set yielded five plausible periods within $0.1 < P < 30$ d: 0.39661(5) d ($\chi^2_{\text{red}} = 2.8$), 0.6585(2) d ($\chi^2_{\text{red}} = 2.5$), 1.90798(71) d ($\chi^2_{\text{red}} = 2.2$), 1.9377(13) d ($\chi^2_{\text{red}} = 4.6$), and 2.0905(12) d ($\chi^2_{\text{red}} = 2.7$). In Fig. 2, we show the Lomb-Scargle periodograms and χ^2 distributions associated with the $\langle B_z \rangle$ and Hipparcos measurements. It is evident that, although similar, the best-fit 1.90798(71) d period, which yields a clear sine variation of $\langle B_z \rangle$ versus phase, is not in agreement with the shorter rotational period identified by Wraight et al. (2012): phasing the $\langle B_z \rangle$ measurements with the 1.8871(8) d period yields significant dispersion between points that are approximately coincident in phase (e.g. $\langle B_z \rangle$ values of -375 ± 18 G and -64 ± 30 G appear separated in phase by < 0.03). The authors note the possible influence of systematic effects on their inferred P_{rot} values, which could potentially explain the discrepancy; however, they suggest that the systematics are unlikely to strongly influence the reported periods.

We adopt $P_{\text{rot}} = 1.90798(71)$ d as it (1) exhibits the closest agreement with one of the two reported photometric periods and (2) corresponds to the minimal χ^2 sinusoidal fit to the $\langle B_z \rangle$ measurements. Further observations are required to eliminate the alternative rotational periods identified here and to verify the adopted value.

4.5 HD 148898

Manfroid, Mathys & Heck (1985) report three plausible rotational periods for HD 148898: 1.79 ± 0.02 d, 2.33 ± 0.02 d, and 4.67 ± 0.08 d. Based on near infrared variability, Catalano, Leone & Kroll (1998) adopted the value of $P_{\text{rot}} = 0.7462(2)$ d reported by Renson & Maitzen (1978). We obtained four new ESPaDOnS Stokes V observations for this star, which we combined with the single measurement published by Kochukhov & Bagnulo (2006). The five high-precision $\langle B_z \rangle$ measurements could not be adequately phased using $P_{\text{rot}} = 1.79 \pm 0.02$ d ($\chi^2_{\text{red}} = 38$); the 0.7462 d, 2.33 d, and 4.67 d periods yield high quality 1st order sinusoidal fits ($\chi^2_{\text{red}} < 0.01$) and are consistent with the derived radii and $v \sin i$ (i.e. $v_{\text{eq}} > v \sin i$ for both periods). Here we adopt $P_{\text{rot}} = 2.3205(2)$ d based on the marginally lower χ^2 value associated with both the $\langle B_z \rangle$ and Hipparcos measurements compared to the longer 4.682(1) d period; however, we emphasize that additional observations are required to more confidently identify the correct P_{rot} .

4.6 HD 151199

We only found one P_{rot} value of HD 151199 reported in the literature: Gokkaya (1970) find that the star exhibits Ca II K line variations having a period of 6.143 d. The $\langle B_z \rangle$ measurements exhibit a number of statistically significant periods with none appearing within 0.3 d of 6.143 d. The $v \sin i$ value and stellar radius derived in Paper I imply a maximum P_{rot} of approximately 2.4 d. We adopt the minimal χ^2 period within $0.4 - 2.5$ d ($P_{\text{rot}} = 1.83317(22)$ d and $\chi^2_{\text{red}} = 1.0$); however additional magnetic, spectroscopic, or photometric measurements are required to verify this value due to the number of periods which yield reasonably high quality sinusoidal fits.

4.7 HD 221760

Four high-precision Stokes V observations of HD 221760 were obtained with ESPaDOnS; the associated $\langle B_z \rangle$ measurements were found to vary from -72 ± 9 G to 57 ± 9 G. The period search analysis performed using the 1st order sinusoidal function yielded a large number of statistically significant periods. None of the possible periods were found to be consistent with the 12 – 13 d rotational periods suggested by van Genderen (1971) and Catalano, Leone & Kroll (1998) based on their detections of photometric variability. Furthermore, the $v \sin i$ value of 22.4 ± 0.7 km s⁻¹ and stellar radius of $3.6 \pm 0.3 R_{\odot}$ derived in Paper I imply a maximum rotational period of ≈ 9.1 d. We find that the $\langle B_z \rangle$ measurements are coherently phased by a period that is one half that of one of the possible periods reported by Catalano, Leone & Kroll (1998) ($P = 12.665$ d/2 = 6.3325 d).

While no additional archived Stokes V observations or published $\langle B_z \rangle$ measurements with sufficiently high precision could be found, 21 archived Stokes I HARPS observations are available. We attempted to obtain additional constraints on HD 221760’s P_{rot} by searching for spectral line variability using the combined HARPS and ESPaDOnS Stokes I observations. No significant line profile variability could be detected (either visually or from equivalent width

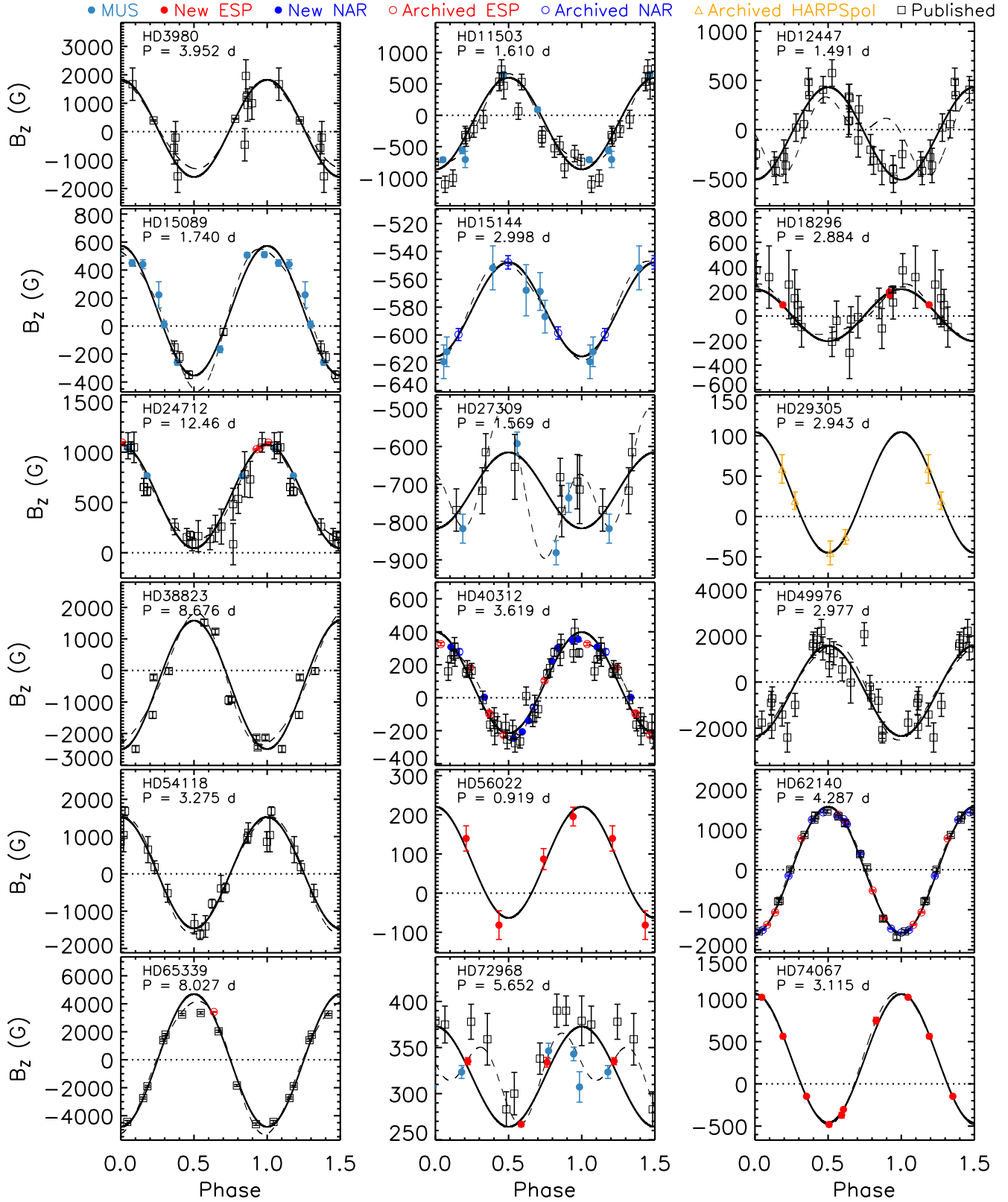


Figure 3. The $\langle B_z \rangle$ measurements used in this analysis phased according to each star’s rotational period – only those mCP stars with known P_{rot} values are shown. The solid black curves and dashed black curves correspond to the best 1st and 2nd order sinusoidal fits (defined by Eqn. 1). Note that the periods listed in each figure are rounded and do not correspond to the actual P_{rot} precision.

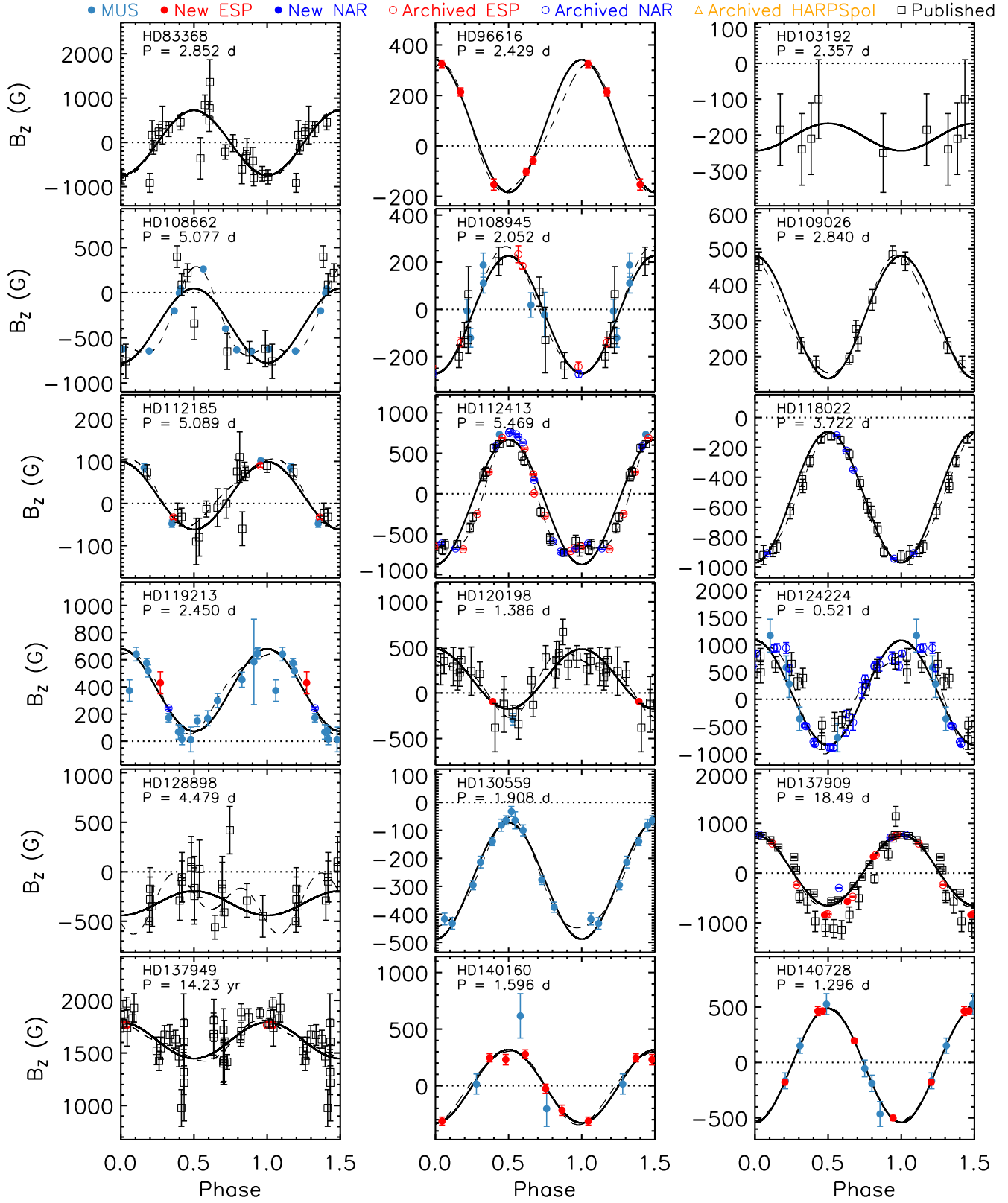


Figure 4. Continued from Fig. 3.

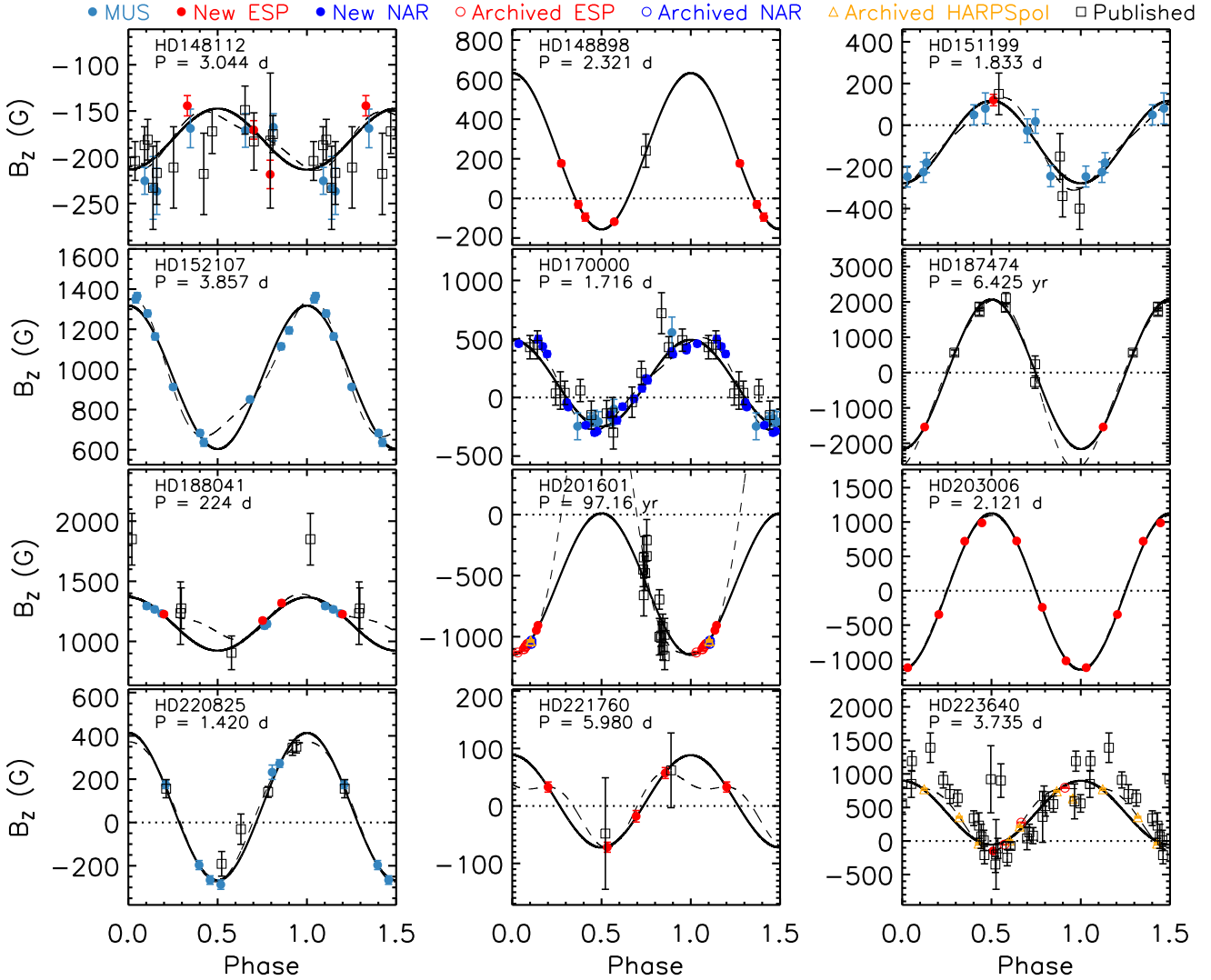
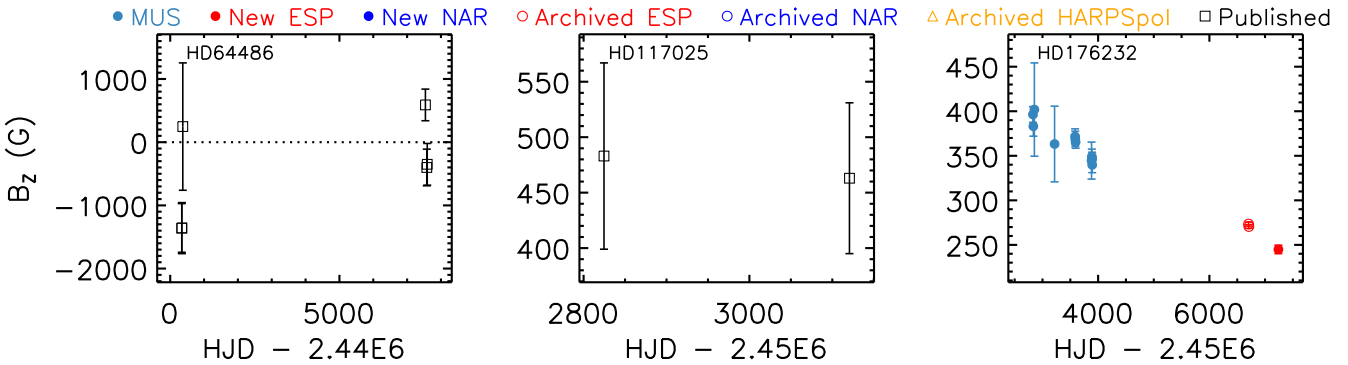


Figure 5. Continued from Fig. 4.

Figure 6. The $\langle B_z \rangle$ measurements used in this analysis associated with those stars with > 1 measurement and without known P_{rot} values.

calculations) from various lines including those associated with Ti, Cr, and Fe.

We adopt $P_{\text{rot}} = 5.98 \pm 0.06$ d based on the preceding discussion, however, we emphasize that further confirmation of this value is required.

4.8 HD 64486, HD 117025, HD 176232, and HD 217522

No published rotational periods were found for these five mCP stars. We were unable to infer the P_{rot} values of HD 64486, HD 117025, or HD 217522 on account of (1)

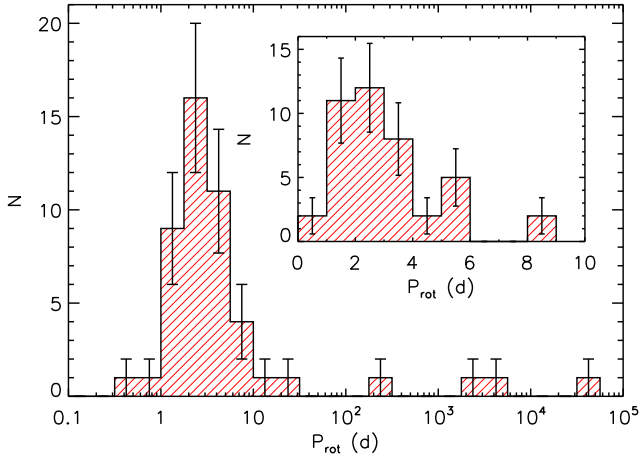


Figure 7. Distribution of rotational periods for 48/52 of the mCP stars. The inset plot shows the same distribution for $P_{\text{rot}} \leq 10$ d.

an insufficient number of available $\langle B_z \rangle$ measurements and (2) the absence of any statistically significant variability in the associated Hipparcos photometric measurements. P_{rot} of HD 176232 could not be derived on account of insufficient phase coverage of its very long rotational period: the available $\langle B_z \rangle$ measurements exhibit an approximately linear decrease from 400 G to 240 G over a 12 yr period. The $\langle B_z \rangle$ measurements as a function of HJD are shown in Fig. 6 (aside from HD 217522, for which only a single measurement was obtained).

4.9 Distribution of Rotational Periods

In Fig. 7, we show the distribution of rotational periods for those 48/52 stars with known values. It is evident that the sample consists of mCP stars exhibiting minimum and maximum periods that are comparable to the known fastest rotators (~ 0.5 d, e.g. Oksala et al. 2010; Grunhut et al. 2012) and slowest rotators ($\gtrsim 100$ yrs, e.g. Mathys 2015). We find that the distribution is consistent with a log-normal distribution (demonstrated by the derived Kolmogorov-Smirnov (KS) test statistic of 0.15 ± 0.25). Fitting a Gaussian function to the distribution yields a mean of 3.1 ± 2.2 . We note that there exists a tail to very long periods, with the longest determined period in our sample being 97 yrs.

We compared the distribution's peak P_{rot} with that yielded by larger previously published surveys. In Fig. 8 of Wolff (1975), the distribution of compiled rotational periods is concentrated below 10 d and exhibits a peak at $P_{\text{rot}} < 3.2$ d; applying the same binning ($\log(\sigma_{P_{\text{rot}}}/\text{d}) = 0.5$) to the periods associated with the volume-limited survey yields the same peak location and sharp decline in the number of stars with $P_{\text{rot}} > 10$ d. More recently, Netopil et al. (2017) reported rotational periods of more than 500 confirmed or candidate mCP stars. We derived a mean of 2.4 d by fitting a Gaussian function to their distribution of reported periods; therefore, the two distributions' peak locations are in agreement within the estimated uncertainty. The preceding discussion suggests that, in terms of the rotational periods, the survey presented here is representative of the larger population of known mCP stars.

Table 3. Parameters associated with the $\langle B_z \rangle$ curves shown in Figures 3 and 4. Columns 1 to 3 list each star’s HD number, adopted or derived rotational period, and the adopted epoch, respectively. References for those rotational periods taken from the literature are listed in the table’s footer; P_{rot} values without references were derived in this study. Columns 4, 5, and 7 list the mean, amplitudes, and reduced χ^2 values associated with the first-order sinusoidal fits sinusoidal (i.e. C_0 and C_1 in Eqn. 1 with $C_2 \equiv 0$). Column 6 lists the r parameters (Eqn. 2 of Preston 1967).

HD (1)	P_{rot} (d) (2)	HJD ₀ – 2.4×10^6 (3)	B_0 (G) (4)	B_1 (G) (5)	r (6)	χ^2_{red} (7)
3980	3.9516(3) ^a	40927.2031	120 ± 1810	1710 ± 4470	−0.87 ± 0.44	1.5
11502	1.60984(1)	43002.93904	−130 ± 230	730 ± 350	−0.69 ± 0.21	3.8
12446	1.4907(12) ^b	43118.3498	−40 ± 84	470 ± 130	−0.84 ± 0.07	0.8
15089	1.74050(3) ^{cd}	53039.89185	109 ± 63	463 ± 90	−0.62 ± 0.10	6.6
15144	2.99799(1)	52254.23776	−581.6 ± 7.2	33.8 ± 9.9	0.89 ± 0.05	0.2
18296	2.88416(15)	42999.22302	10 ± 210	210 ± 340	−0.94 ± 0.16	0.7
24712	12.4580(15) ^e	47179.9838	560 ± 160	510 ± 250	0.04 ± 0.39	3.6
27309	1.5688840(47) ^f	52247.1353483	−716 ± 80	100 ± 120	0.75 ± 0.43	3.0
29305	2.943176(3) ^g	56967.257773	29.9 ± 1.3	74.7 ± 1.3	−0.43 ± 0.01	< 0.1
38823	8.676(30)	51894.778	−460 ± 430	2040 ± 640	−0.63 ± 0.16	24.7
40312	3.61866(2)	42762.85334	91 ± 44	307 ± 62	−0.54 ± 0.12	9.9
49976	2.97666(8) ^h	41401.97078	−380 ± 610	1960 ± 830	−0.68 ± 0.20	3.2
54118	3.27535(10) ⁱ	42114.75746	30 ± 250	1500 ± 330	−0.96 ± 0.01	1.5
56022	0.91889(3) ^g	57324.95641	79 ± 39	142 ± 75	−0.29 ± 0.37	1.1
62140	4.28677(3)	50505.89765	−5 ± 57	1577 ± 77	−0.993 ± 0.001	13.7
65339	8.02681(4) ^j	50494.99521	−50 ± 540	4740 ± 840	−0.978 ± 0.006	58.8
72968	5.6525(10)	52251.9491	318 ± 40	54 ± 66	0.71 ± 0.49	6.1
74067	3.11511(226)	57326.88599	301 ± 38	761 ± 46	−0.43 ± 0.04	1.6
83368	2.851976(3) ^k	45063.924739	−10 ± 260	730 ± 410	−0.97 ± 0.03	1.7
96616	2.42927(2)	57356.54706	79 ± 18	263 ± 25	−0.54 ± 0.06	0.8
103192	2.35666(2) ⁱ	43736.07566	−206 ± 68	38 ± 99	0.7 ± 1.2	0.3
108662	5.07735(24)	42214.90968	−360 ± 210	410 ± 300	−0.06 ± 0.61	53.5
108945	2.05186(12)	51613.95547	−23 ± 77	250 ± 100	−0.83 ± 0.11	1.2
109026	2.84(22) ^l	56336.96	309 ± 19	170 ± 29	0.29 ± 0.13	0.7
112185	5.0887(13) ^{mn}	41794.5148	19 ± 36	80 ± 45	−0.62 ± 0.31	1.9
112413	5.46913(8)	50503.70120	−104 ± 96	770 ± 120	−0.76 ± 0.06	184.8
118022	3.722084(2) ^h	50499.616970	−533 ± 55	438 ± 68	0.10 ± 0.14	2.2
119213	2.4499141(38) ^o	53406.2587031	380 ± 110	300 ± 120	0.11 ± 0.37	2.6
120198	1.38576(80) ^p	42769.49376	150 ± 210	330 ± 260	−0.36 ± 0.61	1.1
124224	0.52070308(120) ^{qr}	42850.85176720	120 ± 180	960 ± 240	−0.78 ± 0.09	7.0
128898	4.4790(1) ^s	42116.9439	−320 ± 180	120 ± 260	0.4 ± 1.4	1.4
130559	1.90798(1)	53407.61250	−280 ± 25	208 ± 32	0.15 ± 0.13	2.0
137909	18.4877(15) ^t	46201.8254	60 ± 150	710 ± 190	−0.84 ± 0.07	104.9
137949	5195	38166	1620 ± 100	170 ± 170	0.81 ± 0.27	1.8
140160	1.59587(11)	51607.01456	−10 ± 150	320 ± 180	−0.97 ± 0.03	1.4
140728	1.29559(2)	53864.86021	−27 ± 35	514 ± 42	−0.90 ± 0.01	0.3
148112	3.04416(112)	52094.28900	−180 ± 23	33 ± 35	0.69 ± 0.46	1.2
148898	2.3205(2)	52764.4371	238 ± 83	390 ± 110	−0.25 ± 0.23	< 0.1
151199	1.83317(22)	53366.50581	−81 ± 65	198 ± 92	−0.42 ± 0.33	0.8
152107	3.857500(15) ^u	53600.975034	961 ± 49	357 ± 64	0.46 ± 0.13	9.8
170000	1.71649(2) ^v	42632.30626	123 ± 60	370 ± 82	−0.50 ± 0.14	4.5
187474	2345(15) ^w	45534	−50 ± 300	2120 ± 420	−0.96 ± 0.01	2.0
188041	224.0(2) ^w	46319.5	1140 ± 210	220 ± 430	0.68 ± 0.79	1.6

continued on next page

continued from previous page

HD	$P_{\text{rot}} (d)$	$\text{HJD}_0 - 2.4 \times 10^6$	$B_0 (G)$	$B_1 (G)$	r	χ_{red}^2
(1)	(2)	(3)	(4)	(5)	(6)	(7)
201601	35462.5(6) ^x	52457.1	-570 ± 560	580 ± 680	-0.0 ± 1.1	1.5
203006	2.12073(135)	57238.62987	-11 ± 48	1137 ± 66	-0.981 ± 0.002	4.8
220825	1.42020(18)	52095.27809	73 ± 46	340 ± 60	-0.65 ± 0.09	1.1
221760	5.98(6)	52790.80	8 ± 15	80 ± 15	-0.82 ± 0.06	< 0.1
223640	3.735239(24) ^y	42828.902150	420 ± 350	480 ± 420	-0.06 ± 0.81	19.3

^a Maitzen, Weiss & Wood (1980), ^b Borra & Landstreet (1980), ^c Musielok et al. (1980)

^d Jasinski, Muciek & Woszczyk (1981), ^e Kurtz (1982), ^f North & Adelman (1995)

^g Heck, Mathys & Manfroid (1987), ^h Catalano & Leone (1994), ⁱ Manfroid & Renson (1994)

^j Hill et al. (1998), ^k Kurtz et al. (1997), ^l Alecian et al. (2014)

^m Deutsch (1947), ⁿ Bohlender & Landstreet (1990), ^o Ziznovsky & Mikulasek (1995)

^p Wade et al. (1998), ^q Pyper et al. (1998), ^r Sokolov (2000)

^s Kurtz et al. (1994), ^t Bagnulo, Landolfi & Degl'Innocenti (1999), ^u Schoneich, Zelvanova & Musielok (1988)

^v Musielok (1986), ^w Mathys (1991), ^x Bychkov, Bychkova & Madej (2016)

^y North, Brown & Landstreet (1992)

4.10 Inclination Angles

For each star in our sample with known P_{rot} , we derived the inclination of the star's rotation axis assuming rigid rotation. The inclination angles were derived according to

$$i = \arcsin \left[\frac{1}{50.6 \text{ km s}^{-1} \text{ days}} \frac{v \sin i}{P_{\text{rot}}} \left(\frac{R}{R_{\odot}} \right)^{-1} \right] \quad (2)$$

using the rotational periods in conjunction with the projected rotational velocities ($v \sin i$) and stellar radii (R) derived or adopted in Paper I. The $v \sin i$ values of those stars with long rotational periods ($P_{\text{rot}} \gtrsim 10 \text{ d}$) could, in general, not be derived and have not been reported in the literature. This is related to the fact that, in these cases, the observed spectral line broadening is dominated by thermal broadening, Zeeman splitting, etc. thus preventing a determination of $v \sin i$ of useful precision. We were able to derive or adopt reported $v \sin i$ values for 43/47 of the stars with known rotational periods. Detailed analyses involving the derivation of i associated with HD 24712 and HD 187474, which both exhibit $v \sin i < 10 \text{ km s}^{-1}$, have been previously published. For HD 24712, we adopt $i = 43 \pm 2^\circ$ derived by Bagnulo et al. (1995) using both circularly and linearly polarized spectra. For HD 187474, we adopt $i = 86^\circ$, which was derived by Landstreet & Mathys (2000) by modelling both $\langle B_z \rangle$ measurements and mean field modulus measurements; no uncertainty is reported. In total, we were able to derive or compile inclination angles for 45/52 of the mCP stars.

In Fig. 8 (top), we show the distribution of the 45 known inclination angles. It is apparent that the distribution is strongly peaked at the $45^\circ < i < 60^\circ$ bin. Such a feature is not associated with a distribution of inclination angles that are randomly oriented in space, which is characterized by a monotonic increase in frequency from 0° to 90° . Furthermore, either an excess of moderate i values ($30^\circ < i < 60^\circ$) or a deficiency of high i values ($i > 60^\circ$) relative to a random distribution is apparent when comparing the cumulative distribution functions (CDFs) of $\sin i$ as shown in Fig. 8 (bottom). We computed a KS test statistic comparing the distribution of i values with that associated with a random distribution (0.19 ± 0.17), which suggests that the inclination angles of the mCP stars in this sample may not be drawn from a random distribution.

Previous studies have addressed the question of whether the inclination angles of mCP stars are in fact randomly oriented in space. Abt (2001) and Netopil et al. (2017) compiled 102 and 180 inclination angles, respectively, and concluded that the resulting distributions are consistent with random distributions. The discrepancy between the observed and expected (random) i distributions in the volume limited survey presented here may be caused by the fact that the observed distribution is incomplete: for 7/52 stars, i could not be derived or found in the literature. We attempted to estimate the statistical significance of the 0.19 ± 0.17 KS test statistic by carrying out a Monte Carlo (MC) simulation. This involved generating 10^5 simulated distributions consisting of 45 i values sampled from the theoretical random distribution. KS test statistics comparing each simulated distribution with the theoretical random distribution were then calculated. We found that 7 per cent of the simulated distributions exhibited a test statistic ≥ 0.19 ; therefore, we con-

clude that the difference between the observed and random distributions is not statistically significant.

Although it is likely that the inclination angles presented here are randomly oriented, we note that the location of the maximum incidence of i shown in Fig. 8 is similar to the location of the distribution's peak found in the results of the larger Abt (2001) and Netopil et al. (2017) studies. In Fig. 1 of Abt (2001), the $\sin i$ distribution peaks at ≈ 0.7 ($i \approx 45^\circ$) while the inclination angles compiled by Netopil et al. (2017) exhibit a maximum frequency within $45^\circ < i < 60^\circ$. This may not be entirely unexpected considering that a number of common mCP stars are included in all three studies: 20 and 21 per cent of the Abt (2001) and Netopil et al. (2017) samples of mCP stars with known i are also included in our volume limited survey. The statistical significance of the position of this peak in our sample was estimated using the results of the MC simulation discussed above. For each of the 10^5 simulated distributions consisting of 45 randomly oriented i values, we determined the location of the maximum incidence when the distribution is binned using $\Delta i = 15^\circ$, as shown in Fig. 8. Nineteen per cent of the simulated distributions exhibited a maximum incidence within $45^\circ < i < 60^\circ$ suggesting that the location of the peak is not statistically significant. We also evaluated the statistical significance of the peak height relative to the neighbouring bins (e.g. the peak shown in Fig. 8 exhibits a peak height of 9 relative to the two neighbouring bins). We found that 7 per cent of the simulated distributions exhibited peaks with relative heights ≥ 9 . Therefore, while the significance of the peak height is higher than that associated with its location, we do not consider it to be statistically significant.

5 MAGNETIC PARAMETERS

The magnetic field strengths and geometries of the mCP stars can be estimated using the ORM (Stibbs 1950). In particular, we use Equations 1 and 2 of Preston (1967) to derive the strength of the field's dipole component (B_d) along with the associated obliquity angle (β , i.e. the angle between the dipole component's axis of symmetry and the star's rotational axis). This derivation depends on the star's inclination angle (i), linear limb-darkening coefficient (u), and ratio of the minimum to maximum longitudinal field strengths ($r \equiv \langle B_z \rangle_{\text{min}} / \langle B_z \rangle_{\text{max}}$).

Linear limb-darkening coefficients were derived using the grid calculated by Díaz-Cordovés, Claret & Gimenez (1995). This grid is calculated for a range of surface gravities ($0.0 \leq \log g \leq 5.0$ [cgs]), effective temperatures ($3500 \leq T_{\text{eff}} \leq 50000 \text{ K}$), and photometric filters (Johnson *UVB* and Strömgren *uvby*). We used the limb-darkening coefficients calculated for the Johnson *V* filter because of the fact that this filter's transmission function approximately spans the wavelength range of the LSD line masks ($3000 \leq \lambda \leq 7000 \text{ Å}$) discussed in Sect. 3.1. The grid of Johnson *V* limb-darkening coefficients was interpolated for each star over $\log g$ and T_{eff} (using the $\log g$ and T_{eff} values derived in Paper I).

The ratios of minimum to maximum field strengths (r) for each star were derived from the fits to the phased $\langle B_z \rangle$ measurements shown in Figures 3 to 5. Both $\langle B_z \rangle_{\text{min}}$ and $\langle B_z \rangle_{\text{max}}$ were calculated using the mean ($B_0 \equiv C_0$) and am-

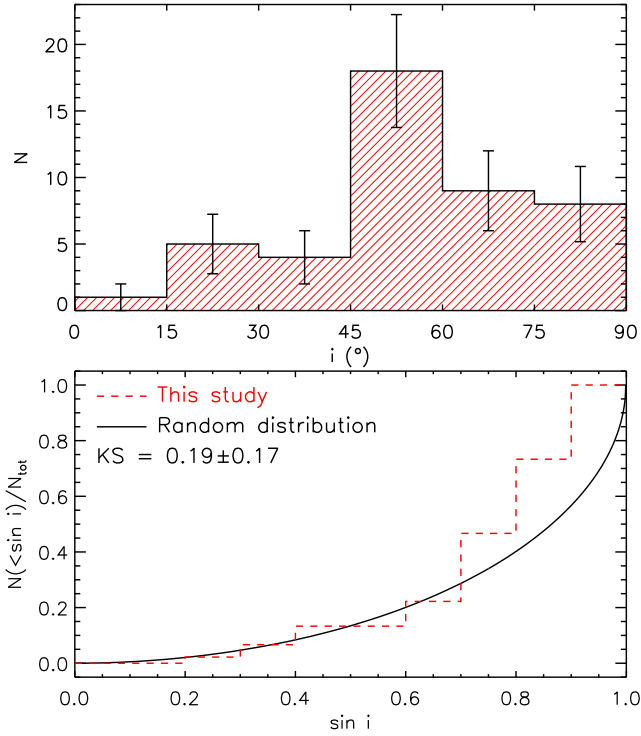


Figure 8. *Top:* Distribution of inclination angles for the 44/52 mCP stars with known $v \sin i$ and known P_{rot} values or with published i values. *Bottom:* Cumulative distribution function of $\sin i$ (dashed red) compared against that associated with a distribution of randomly oriented rotational axes (solid black). The Kolmogorov-Smirnov test statistic of $KS = 0.19 \pm 0.17$ suggests that the inclination angles may not be distributed randomly.

plitudes ($B_1 \equiv C_1$) associated with the 1st order sinusoidal fits (i.e. Eqn. 1 with $C_2 \equiv 0$). The uncertainties in B_0 and B_1 (and thus, in r) were derived by applying the method of residual bootstrapping. The method involves calculating the residuals associated with the $\langle B_z \rangle$ measurements and the (1st order) sinusoidal fit. For each $\langle B_z \rangle$ measurement, we add to it a randomly selected residual and the sinusoidal fit is recalculated. This process is repeated 10 000 times yielding approximately Gaussian fitting parameter distributions, which are used to estimate 3σ uncertainties.

Finally, B_d and β were derived using the calculated values of i , u , and r according to Equations 1 and 2 of Preston (1967). Given the number of parameters involved in this derivation (e.g. T_{eff} , R , $v \sin i$, etc.), it is difficult to evaluate how they are correlated. Without accounting for these correlations, the uncertainties in B_d and β will likely be erroneously high. We estimated σ_{B_d} and σ_β by extending the Monte Carlo (MC) uncertainty analysis carried out in Paper I. This involved calculating each star's B_d and β for $\gtrsim 1000$ data points each consisting of randomly selected effective temperatures and luminosities normally distributed according to their most probable values and their uncertainties (Shultz et al., in prep; a brief description is presented in Paper I). This analysis was extended by assigning $v \sin i$ and r values – randomly generated from normal distributions with widths defined by $\sigma_{v \sin i}$ and σ_r – to each of the previously generated MC data points. Ultimately, this method yields distributions of B_d and β values, which can be used to infer

σ_{B_d} and σ_β . In general, the resulting distributions are either positively or negatively skewed. Therefore, rather than defining σ_{B_d} and σ_β using each distribution's standard deviation, we adopt minimum and maximum limits defined such that 99.7 per cent of the distribution is enclosed.

In six cases (HD 3980, HD 38823, HD 108662, HD 108945, HD 137909, and HD 223640) the most probable $v \sin i$ values derived in Paper I were found to exceed the equatorial velocities (v_{eq}) calculated using P_{rot} , and R ; however, the $v \sin i$ and v_{eq} values of all six stars were found to be equal within the estimated uncertainties (i.e. they are consistent with $i \approx 90^\circ$). In these cases, we removed those MC data points for which $v \sin i > v_{\text{eq}}$. The peak values of the resulting MC distributions were then used to define new, most probable $v \sin i$ values.

5.1 Dipole Field Strengths

In Fig. 9, we show the derived dipole field strengths for 45/52 mCP stars in the sample (i.e. those with known rotational periods and inclination angles and for which multiple $\langle B_z \rangle$ measurements are available). The B_d distribution is well characterized by a log-normal distribution as demonstrated by the derived KS test statistic of 0.10 ± 0.19 . Fitting a Gaussian function to $\log(B_d/G)$ yields a mean and 3σ uncertainty of 3.4 ± 0.2 (corresponding to $2.6^{+1.9}_{-1.1}$ kG). The maximum derived B_d in the sample corresponds to $18.1^{+3.4}_{-2.7}$ kG (HD 65339), which is in agreement with the value reported by Landstreet (1988). The minimum derived B_d corresponds to 330^{+80}_{-60} G (HD 112185); however, the minimum dipole field strength derived when considering the upper B_d error limits corresponds to $B_d^{\text{max}} = 390$ G (HD 221760).

The survey carried out by Aurière et al. (2007) was specifically designed to search for mCP stars hosting weak dipole fields. They reported a minimum most probable field strength (i.e. minimum B_d without considering the estimated lower error limits) of 100 G. The minimum B_d^{max} found in their study is 477 G, which is slightly higher but still comparable to that derived here. The fact that they did not find any dipole field strengths $\lesssim 100$ G led them to propose the existence of a critical dipole field strength (B_c), which defines a minimum field strength necessary for a field to maintain stability. They estimate that $B_c \approx 300$ G for a typical A-type star and is indicated in Fig. 9; it is clear that the majority of the 45 B_d values derived for the stars in our volume limited survey greatly exceed 300 G.

Aurière et al. (2007) derived the following expression for the order of magnitude of B_c in terms of P_{rot} , R , T_{eff} , and the equipartition field strength of a typical main sequence (MS) A-type star ($B_{\text{eq}} = 170$ G):

$$B_c \sim 2B_{\text{eq}} \left(\frac{P_{\text{rot}}}{5 \text{ d}} \right)^{-1} \left(\frac{R}{3 R_\odot} \right) \left(\frac{T}{10^4 \text{ K}} \right)^{-1/2}. \quad (3)$$

We derived B_d/B_c for each of the 45 stars having estimated dipole field strengths. All 45 stars exhibit $B_d/B_c \gtrsim 1$; four stars were found to have most probable $B_d/B_c \in [0.6, 1)$. Three of these four stars (HD 29305, HD 56022, and HD 112185) have an estimated B_d/B_c upper error limit < 1 and therefore serve as the best candidates in our sample for either (1) potentially disproving the hypothesis that field strengths must exceed B_c or (2) refining the value of B_c .

The derivation of B_c by Aurière et al. (2007) applies

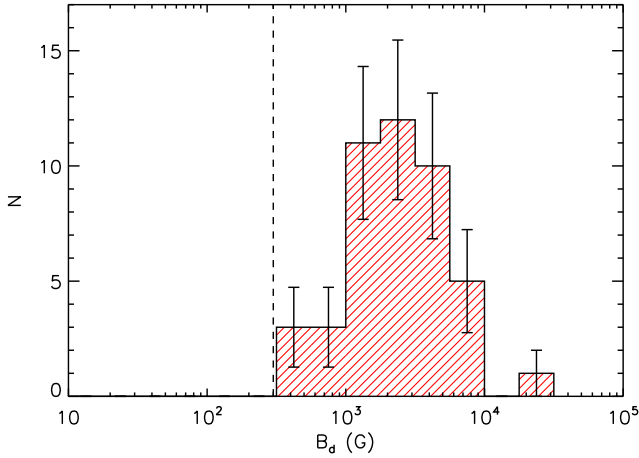


Figure 9. Distribution of dipole magnetic field strengths for 45/52 of the mCP stars. The vertical dashed line corresponds to the critical field strength of a typical MS A-type star ($B_c = 300$ G) estimated by Aurière et al. (2007).

to all A-type stars spanning the main sequence. Therefore, an additional test of the existence of B_c can be carried out by estimating each mCP stars' B_d/B_c value as a function of fractional MS age (τ) and determining if $B_d/B_c \ll 1$ at any point during its evolution across the MS. We estimated each stars' $R(\tau)$ and $T_{\text{eff}}(\tau)$ by interpolating evolutionary tracks computed by Ekström et al. (2012) and Mowlavi et al. (2012), which is discussed more thoroughly in Paper I. The change in P_{rot} occurring across the MS was estimated using two grids of rotating evolutionary tracks. For stars with masses $< 1.7 M_\odot$, we used the rotating solar metallicity ($Z = 0.014$) evolutionary tracks computed by Ekström et al. (2012) for v_{eq}/v_c equal to 0.0 and 0.4 where v_{eq} and v_c are the equatorial velocity and critical breakup rotational velocity at the zero age MS (ZAMS). For stars with masses $\geq 1.7 M_\odot$, we used the higher v_{eq}/v_c density ($v_{\text{eq}}/v_c = 0.0, 0.1, 0.3, 0.5, 0.6, 0.7, 0.9, \text{ and } 1.0$) solar metallicity grids computed by Georgy et al. (2013). The change in the dipole field strength was estimated by assuming that magnetic flux is conserved. Under this assumption, B_d decreases with R^{-2} as R increases from the ZAMS to the terminal age MS (TAMS). We find that the predicted B_d/B_c values decrease monotonically along the MS; as a result, only one of the 45 stars with derived B_d values is predicted to have $B_d/B_c < 1$ at earlier points during its MS lifetime. The distributions of the observed B_d/B_c and the B_d/B_c values predicted at the ZAMS are shown in Fig. 10.

It is evident that both of the observed and predicted ZAMS B_d/B_c distributions shown in Fig. 10 exhibit a sharp decrease in frequency at $B_d/B_c < 1$. This is consistent with the notion that the current B_d/B_c values are initially drawn from a wider distribution containing lower B_d/B_c values: the initial distribution is truncated at $B_d/B_c = 1$ resulting in a sharp decline towards lower values.

5.2 Obliquity Angles

In Fig. 11, we show the distribution and CDF associated with the 45 obliquity angles (β) derived using Equation 3 of Preston (1967). The β distribution exhibits a moderate in-

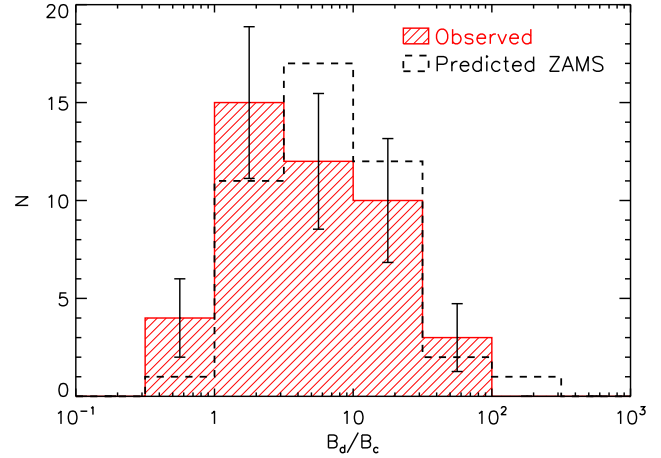


Figure 10. Distribution of the ratio of B_d to the critical field strength (B_c) derived by Aurière et al. (2007); these authors hypothesize that no A-type stars should be found exhibiting $B_d/B_c < 1$ (indicated by the vertical dashed line).

crease from low to high β values, which is qualitatively similar to that associated with a distribution of randomly oriented axes. A more quantitative comparison was carried out using the CDFs of the derived $\sin \beta$ and theoretical random distributions. We derived a KS test statistic of 0.17 ± 0.15 suggesting that the β values may not be randomly oriented. The significance of this KS test statistic was evaluated using the same Monte Carlo simulation that was carried out in Sect. 4.10 with the inclination angles. 10^5 simulated distributions were generated, each consisting of 45 β values drawn from the theoretical random distribution. A KS test statistic comparing each of the simulated random distributions with the theoretical random distribution were calculated. We found that 13 per cent of the resulting KS values were ≥ 0.17 ; therefore, we conclude that the apparent difference between the derived β values and the theoretical random distribution is statistically insignificant.

6 EVOLUTION OF MAGNETIC FIELD STRENGTH

In Paper I, we identified statistically significant trends in the average surface chemical abundances of certain elements (e.g. Si, Ti, Cr, and Fe) as functions of stellar age. Similar correlations between the atmospheric chemical abundances and ages of Bp stars have been previously reported by Bailey, Landstreet & Bagnulo (2014). The authors also found that the same elements exhibiting coherent changes with age also exhibit changes with the measured magnetic field strengths; this is attributed to a decrease in field strength with age as previously reported by Landstreet et al. (2007, 2008) for both MS Ap and Bp stars ($8 < T_{\text{eff}} < 20$ kK).

In Fig. 12, we plot R , B_d , and $B_d R^2$ (i.e. the surface magnetic flux) as functions of age ($\log t/\text{yrs}$) and fractional MS age (τ). The 45 mCP stars represented in the figure are divided into low-mass ($M/M_\odot < 2$), intermediate-mass ($2 \leq M/M_\odot < 3$), and high-mass ($M/M_\odot \geq 3$) ranges. This is done for two reasons: (1) the increase in R as each star evolves across the MS increases with mass; and (2) the

Table 4. Parameters associated with the magnetic field geometries and strengths. Columns 2 to 3 list the inclination angles and obliquity angles. Columns 4 to 6 list the dipole field strengths (B_d), critical field strengths (B_c), and ratios of B_d to B_c .

HD	i (°)	β (°)	B_d (G)	B_c (G)	B_d/B_c
(1)	(2)	(3)	(4)	(5)	(6)
3980	84^{+4}_{-32}	84^{+3}_{-82}	6360^{+57570}_{-5570}	285^{+41}_{-33}	22^{+206}_{-19}
11502	76^{+13}_{-24}	54^{+27}_{-50}	3000^{+29130}_{-750}	652^{+139}_{-99}	$4.6^{+47.9}_{-1.4}$
12446	38^{+13}_{-9}	86^{+3}_{-4}	2450^{+710}_{-520}	1010^{+220}_{-190}	$2.4^{+0.5}_{-0.4}$
15089	56^{+23}_{-14}	71^{+8}_{-30}	1850^{+490}_{-160}	725^{+69}_{-61}	$2.5^{+0.7}_{-0.3}$
15144	20 ± 5	9^{+3}_{-2}	1951^{+73}_{-45}	425^{+42}_{-38}	$4.6^{+0.6}_{-0.5}$
18296	29^{+12}_{-9}	$89.0^{+0.4}_{-13.7}$	1430^{+1090}_{-830}	567^{+119}_{-99}	$2.5^{+1.8}_{-1.5}$
24712	43^{+11}_{-10}	45^{+11}_{-12}	3340^{+380}_{-280}	96^{+7}_{-6}	$34.5^{+4.6}_{-4.0}$
27309	49^{+16}_{-10}	7 ± 4	3600^{+1980}_{-580}	780^{+140}_{-120}	$4.6^{+3.4}_{-1.3}$
29305	54^{+16}_{-11}	61^{+8}_{-19}	349^{+44}_{-4}	564^{+61}_{-58}	$0.6^{+0.1}_{-0.1}$
38823	80^{+7}_{-53}	71^{+11}_{-63}	7590^{+39130}_{-460}	114^{+20}_{-13}	67^{+324}_{-11}
40312	63^{+22}_{-13}	59^{+12}_{-45}	1291^{+2800}_{-94}	724^{+68}_{-63}	$1.8^{+4.1}_{-0.2}$
49976	69^{+18}_{-29}	63^{+20}_{-57}	7530^{+48620}_{-1690}	382^{+46}_{-43}	$19.7^{+134.5}_{-4.6}$
54118	58^{+27}_{-15}	$88.2^{+0.1}_{-15.2}$	5810^{+1380}_{-960}	432^{+50}_{-43}	$13.4^{+3.1}_{-2.1}$
56022	50^{+26}_{-17}	56^{+15}_{-34}	712^{+476}_{-91}	1252^{+88}_{-85}	$0.6^{+0.4}_{-0.1}$
62140	70^{+18}_{-19}	$89.5^{+0.2}_{-11.8}$	5110^{+1050}_{-330}	349^{+68}_{-58}	$14.6^{+2.0}_{-1.6}$
65339	55^{+18}_{-11}	$89.1^{+0.7}_{-3.9}$	18120^{+3540}_{-2700}	186 ± 22	97^{+15}_{-11}
72968	51^{+18}_{-11}	8 ± 5	1620^{+1250}_{-290}	241^{+36}_{-33}	$6.7^{+6.5}_{-1.8}$
74067	58^{+28}_{-20}	57^{+15}_{-48}	3439^{+12198}_{-70}	440^{+55}_{-49}	$7.8^{+28.8}_{-0.8}$
83368	69^{+17}_{-10}	$87.7^{+0.0}_{-31.3}$	2400^{+540}_{-470}	453^{+42}_{-36}	$5.3^{+1.1}_{-1.1}$
96616	74^{+14}_{-20}	44^{+24}_{-39}	1260^{+7780}_{-210}	693^{+89}_{-80}	$1.8^{+11.8}_{-0.5}$
103192	60^{+14}_{-9}	6^{+6}_{-5}	1380^{+1080}_{-320}	856^{+104}_{-92}	$1.6^{+1.6}_{-0.5}$
108662	80^{+8}_{-32}	17^{+30}_{-16}	3110^{+54640}_{-770}	238^{+31}_{-28}	$12.5^{+225.1}_{-3.2}$
108945	80^{+9}_{-26}	80^{+7}_{-73}	870^{+4980}_{-150}	782^{+58}_{-56}	$1.1^{+6.3}_{-0.2}$
109026	15^{+8}_{-6}	65^{+10}_{-12}	2480^{+1590}_{-660}	490^{+190}_{-130}	$5.0^{+2.6}_{-1.2}$
112185	56^{+16}_{-11}	71^{+12}_{-21}	327^{+79}_{-62}	460^{+43}_{-42}	$0.7^{+0.2}_{-0.1}$
112413	48^{+35}_{-21}	82^{+4}_{-42}	3460^{+2290}_{-690}	245^{+39}_{-36}	$14.1^{+8.8}_{-3.2}$
118022	27^{+6}_{-5}	58^{+6}_{-7}	3650^{+610}_{-370}	308 ± 22	$11.9^{+2.0}_{-1.3}$
119213	60^{+27}_{-26}	25^{+24}_{-23}	2620^{+28240}_{-660}	497^{+77}_{-66}	$5.3^{+58.8}_{-1.8}$
120198	48^{+11}_{-8}	63^{+13}_{-16}	1600^{+410}_{-360}	890^{+140}_{-120}	$1.8^{+0.5}_{-0.4}$
124224	46^{+10}_{-8}	82^{+4}_{-5}	4460^{+780}_{-630}	2020^{+240}_{-200}	$2.2^{+0.3}_{-0.3}$
128898	42^{+7}_{-6}	23^{+15}_{-16}	1430^{+310}_{-270}	266^{+22}_{-20}	$5.4^{+1.5}_{-1.1}$
130559	18^{+6}_{-5}	67^{+6}_{-7}	2360^{+770}_{-440}	716^{+100}_{-89}	$3.3^{+1.0}_{-0.6}$
137909	84^{+5}_{-27}	75^{+11}_{-70}	2380^{+25570}_{-230}	111^{+17}_{-16}	$19.7^{+220.0}_{-2.3}$
137949	-	-	-	0.27 ± 0.03	-
140160	60^{+18}_{-11}	$88.4^{+0.1}_{-20.7}$	1180^{+290}_{-260}	811^{+69}_{-62}	$1.5^{+0.3}_{-0.3}$
140728	46^{+13}_{-10}	87^{+1}_{-3}	2300^{+460}_{-360}	1080^{+170}_{-140}	$2.1^{+0.3}_{-0.3}$
148112	58^{+27}_{-16}	6 ± 6	1090^{+5680}_{-340}	650^{+83}_{-79}	$1.7^{+9.3}_{-0.7}$
148898	30 ± 5	71^{+4}_{-5}	2580^{+440}_{-330}	802^{+67}_{-62}	$3.2^{+0.5}_{-0.4}$
151199	61^{+23}_{-13}	53^{+14}_{-42}	880^{+2010}_{-140}	684^{+87}_{-80}	$1.3^{+3.1}_{-0.3}$
152107	50^{+17}_{-12}	17 ± 8	4930^{+3040}_{-690}	359 ± 22	$13.7^{+8.8}_{-2.3}$
170000	48^{+5}_{-4}	70^{+4}_{-5}	1750^{+140}_{-160}	1142^{+49}_{-56}	$1.5^{+0.1}_{-0.1}$
187474	86^{+3}_{-32}	72^{+16}_{-42}	7210^{+6310}_{-710}	$0.62^{+0.10}_{-0.08}$	11590^{+9550}_{-1810}
188041	-	-	-	$6.36^{+0.71}_{-0.65}$	-
201601	-	-	-	0.038 ± 0.003	-
203006	51^{+18}_{-11}	$89.3^{+0.6}_{-1.5}$	4640^{+890}_{-750}	653^{+118}_{-100}	$7.1^{+1.0}_{-0.8}$
220825	40^{+10}_{-9}	80^{+3}_{-5}	1700^{+400}_{-260}	722^{+79}_{-66}	$2.4^{+0.5}_{-0.3}$
221760	47^{+9}_{-7}	84^{+4}_{-5}	343^{+47}_{-43}	373^{+34}_{-33}	0.9 ± 0.1
223640	84^{+5}_{-28}	12^{+27}_{-12}	$3740^{+128220}_{-1030}$	315^{+37}_{-35}	$11.3^{+395.1}_{-3.3}$

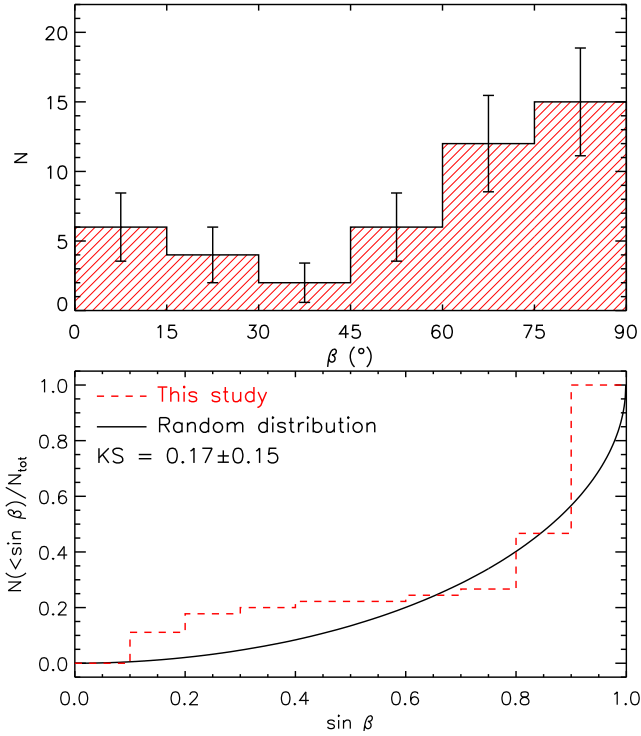


Figure 11. *Top:* Distribution of obliquity angles for the 45/52 mCP stars with known P_{rot} and i values and for which multiple $\langle B_z \rangle$ measurements are *Bottom:* Cumulative distribution function of $\sin \beta$ (dashed red) compared against that associated with a distribution of randomly oriented magnetic dipole axes (solid black). The Kolmogorov-Smirnov test statistic of $KS = 0.17 \pm 0.15$ suggests that the inclination angles may not be distributed randomly.

width of the MS spanned by each of the three mass ranges decreases with decreasing mass. Therefore, under the assumption that magnetic flux is conserved, we expect to see larger changes in B_d with age in the high-mass range compared to the low-mass range. This can result in an increase in the dispersion of B_d and $B_d R^2$ with increasing τ thereby decreasing our ability to detect such evolutionary changes.

The best fitting linear functions were derived for each of the B_d and $B_d R^2$ values associated with the three mass intervals. We used an unweighted least-squares analysis because of the fact that the errors associated with B_d , $\log t/\text{yrs}$, and τ are typically large and asymmetric: B_d diverges as $|i - \beta| \rightarrow 90^\circ$ while $\log t/\text{yrs}$ and τ are significantly more uncertain closer to the ZAMS than to the TAMS (e.g. see Fig. 4 of Kochukhov & Bagnulo 2006). We found that the resulting fits yielded lower residuals compared to those obtained by considering both x and y uncertainties (e.g. using the method described by Williams, Bureau & Cappellari 2010). We estimated 1σ uncertainties in the fitting parameters by bootstrapping the residuals. The resulting linear fits are shown in Fig. 12 and the slopes are listed in Table 5.

We find that the dipole field strengths associated with all three of the mass intervals decrease over both $\log t/\text{yrs}$ and τ ; we do not detect any changes in the magnetic flux ($B_d R^2$) with stellar age. We note that the uncertainties in R are relatively small ($\lesssim 15$ per cent) and that the estimated uncertainties in the slopes associated with B_d and

Table 5. Slopes and 1σ uncertainties associated with the linear fits shown in Fig. 12.

$\log B_d/G$		
Mass Interval	$\log(t/\text{yrs})$ Slope	τ Slope
$M/M_\odot < 2$	-0.90 ± 0.43	-0.62 ± 0.53
$2 \leq M/M_\odot < 3$	-0.29 ± 0.35	-0.65 ± 0.34
$M/M_\odot \geq 3$	-0.89 ± 0.40	-0.75 ± 0.35

$\log [(B_d/G)(R/R_\odot)^2]$		
Mass Interval	$\log(t/\text{yrs})$ Slope	τ Slope
$M/M_\odot < 2$	-0.53 ± 0.54	-0.06 ± 0.59
$2 \leq M/M_\odot < 3$	-0.02 ± 0.36	-0.19 ± 0.31
$M/M_\odot \geq 3$	-0.04 ± 0.42	-0.04 ± 0.36

$B_d R^2$ are comparable (particularly for the slopes involving τ). This suggests that the apparent differences in the rates of change of the field strength and the magnetic flux are not related to the uncertainty introduced by R . Therefore, we conclude that these results are statistically consistent with the notion that magnetic flux is conserved as an mCP star evolves across the MS.

The fact that B_d appears to decrease with increasing stellar age is qualitatively consistent with the findings of Landstreet et al. (2007), whose survey only consisted of cluster members with well-constrained ages. Moreover, the rate of field strength decline that they derived for stars having $3 \leq M/M_\odot \leq 4$ (-0.42 ± 0.14) is consistent with that derived here for our sample's high-mass stars (-0.89 ± 0.40). This agreement provides evidence in support of the notion that the magnetic fields of MS mCP stars decay with age. The rate of change of magnetic flux for the same mass intervals are also in agreement within the uncertainties: Landstreet et al. (2007) derived a slope of -0.22 ± 0.14 while we obtained -0.04 ± 0.42 . Despite the quantitative agreement, it is noteworthy that Landstreet et al. (2007) detect a decrease in magnetic flux over time whereas, for our sample, we do not. It is clear that our sample includes significantly fewer high-mass stars (7 compared to 25) and that the derived ages have a much higher uncertainty. On the other hand, the B_d values associated with the majority of the stars in our sample have been derived from reasonably well sampled $\langle B_z \rangle$ curves; for most of the stars included in the Landstreet et al. (2007) study, only single $\langle B_z \rangle$ measurements were obtained. The data set presented here can be used to assess the significance of this final point.

We carried out an MC simulation in which the magnetic field strengths of the stars in our sample were estimated using only a small number of randomly sampled $\langle B_z \rangle$ measurements. This involved generating 10^4 simulated data sets consisting of either 1 or 3 $\langle B_z \rangle$ measurements for each of the 45 stars with known B_0 and B_1 (i.e. the mean and amplitude characterizing the $\langle B_z \rangle$ curves). The $\langle B_z \rangle$ measurements were generated using random phase values ($\theta \in [0, 1]$) along with B_0 and B_1 such that $\langle B_z \rangle(\theta) = B_0 + B_1 \sin \theta$. Each star's root-mean square field strength (B_{rms}) was then

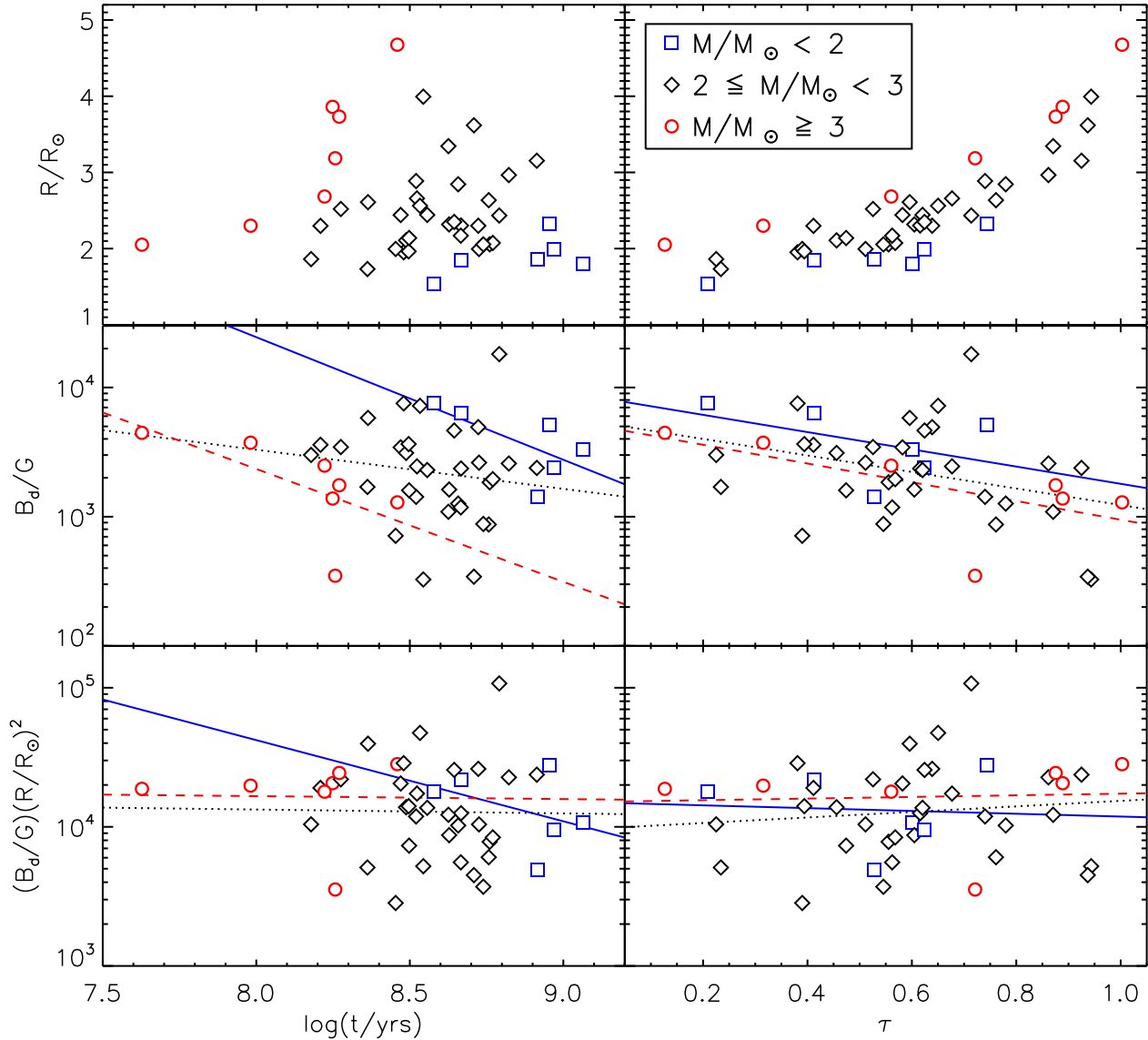


Figure 12. Radius (R , top row), dipole field strength (B_d , middle row), and $B_d R^2$ (bottom row) for 45/52 of the mCP stars in the sample as functions of logarithmic stellar age ($\log t/\text{yrs}$, left column) and fractional MS age (τ , right column). Three mass ranges are identified: $M/M_\odot < 2$, $2 \leq M/M_\odot < 3$, and $M/M_\odot \geq 3$. The lines correspond to the best fitting linear functions for the low-mass (solid blue), intermediate-mass (dotted black), and high-mass (dashed red) stars. The derived slopes and their uncertainties are listed in Table 5.

calculated (as done by Landstreet et al. 2007). Finally, the linear fitting analyses involving $\log t/\text{yrs}$, B_{rms} , and $B_{\text{rms}} R^2$ were carried out and the derived slopes were compared with those generated using the original data set. In Fig. 13, we show the resulting distributions based on the $B_{\text{rms}} R^2$ slopes.

The results of the MC simulation suggest that both the slopes of B_{rms} and $B_{\text{rms}} R^2$ as functions of $\log t/\text{yrs}$ and τ are biased towards lower values when B_{rms} is derived from a small number of $\langle B_z \rangle$ measurements. However, we find that the bias is small and decreases with increasing sample size. Considering the large sample size of the survey carried out by Landstreet et al. (2007), the bias is likely negligible as assumed by the authors. It is clear from the distributions shown in Fig. 13 that, depending on the number of $\langle B_z \rangle$ measurements used to derive B_{rms} of each star, the uncer-

tainty in the slope may be significantly affected. We note that the MC simulation uses the stellar ages derived for the current sample in Paper I; therefore, the results of the simulation are certainly affected by the large age uncertainties to some extent.

It is plausible that the lack of detection of flux decay in our sample could result from (1) a small sample size for each of the mass bins (in particular for the high-mass stars which are expected to exhibit the largest decrease) and (2) large errors in the stellar ages. Additionally, it is noted that, in terms of both $\log t/\text{yrs}$ and τ , the mCP stars in our sample are generally older than those contained in the Landstreet et al. (2007) sample: the fraction of stars having $\tau < 0.4$ is > 50 per cent in the Landstreet et al. (2007) sample compared with 15 per cent in our volume-limited sample. In Fig. 4

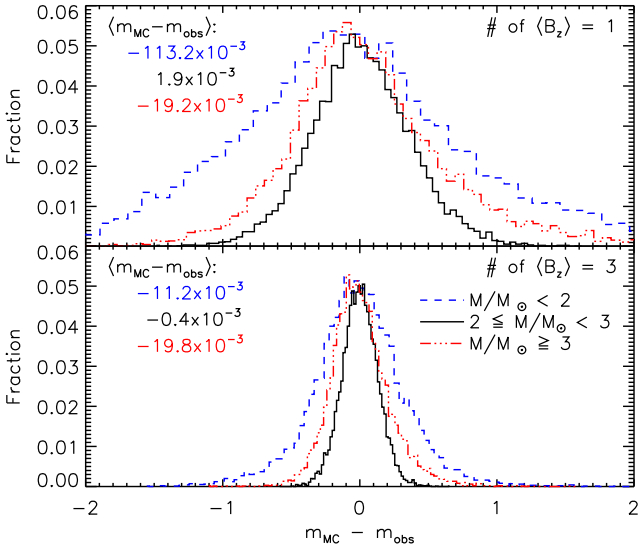


Figure 13. Distributions comparing the slope of $B_{\text{rms}} R^2$ as a function of $\log t/\text{yr}$ generated from the MC simulated data sets with that generated from the original data set. The top distribution corresponds to the B_{rms} values calculated using 1 randomly generated $\langle B_z \rangle$ measurement while the bottom distribution uses 3 measurements. The mean values of each distribution ($\langle m_{\text{MC}} - m_{\text{obs}} \rangle$) are listed in order of increasing mass.

of Landstreet et al. (2008) it is apparent that the rate of flux decay associated with high-mass Ap stars is significantly higher for $\tau < 0.2$ compared with $\tau > 0.2$. This suggests that the apparent discrepancy in terms of the detection of flux decay between our sample and that of Landstreet et al. (2007) may be caused by a decay rate that is higher for younger MS stars coupled with the different age distribution of our sample.

7 DISCUSSION AND CONCLUSIONS

In Paper I, we presented an analysis of the fundamental properties and chemical abundances of 52 and 45 confirmed mCP stars, respectively, located within a distance of 100 pc. This study is the first of its kind in two specific ways. First, it is focused on a volume-limited sample and thus, is less affected by the biases inherent to previous studies of samples of mCP stars (e.g. Kochukhov & Bagnulo 2006; Hubrig, North & Schöller 2007). Secondly, we have attempted to perform the analysis in a homogeneous manner such that any dispersion introduced by using varying techniques or theoretical models is minimized. The results presented here build on those of Paper I with the addition of an analysis of the confirmed mCP stars' rotational periods and magnetic properties. In the following, we discuss these results and present our conclusions.

Rotational periods for 48/52 of the confirmed mCP stars in the sample were adopted based on (1) the available $\langle B_z \rangle$ measurements (i.e. newly obtained or unpublished measurements using ESPaDOnS, NARVAL, and MuSiCoS, newly analyzed measurements, and previously published measurements) and (2) previously published values typically derived from photometric variability. In general, we found

that the rotational periods inferred from magnetic measurements are consistent with the published values. However, in several cases P_{rot} could not be identified unambiguously and we adopted P_{rot} values based on somewhat unreliable or tenuous evidence (e.g. the newly obtained $\langle B_z \rangle$ measurements of HD 221760 were insufficient to derive a unique period and poor agreement was found with previously published values). Adopting unconfirmed rotational periods of certain stars in the sample may have contributed to the detection of an unusual and unexpected feature in the distribution of inclination angles.

The feature in question is the large peak i frequency occurring within 45 to 60° , which also corresponds to the distribution's global peak value. This is unexpected since it is not typically found in a distribution of i values that are randomly oriented in space (e.g. Abt 2001). Although statistically insignificant based on an estimated p-value of 0.07, it is perhaps noteworthy that a similar feature is found in the much larger data set of mCP i values published by Netopil et al. (2017). We note that the distribution shown in Fig. 8 is incomplete since the i values of 7/52 sample stars could not be derived; however, their inclusion is unlikely to dramatically reduce the feature's statistical significance. No correlation between $\sin i$ and Galactic latitude is found (e.g. Fig. 2 of Abt 2001), suggesting that the origin of the unexpected feature found in the i distribution is unlikely to be environmentally dependent.

Landstreet & Mathys (2000) derived β values for a sample of 24 Ap stars and found that the slow rotators ($P_{\text{rot}} > 25$ d) tend to exhibit low β values while only 2 faster rotators in their sample ($P_{\text{rot}} < 25$ d) were found with $\beta < 60^\circ$. Our sample consists of 5 stars with $P_{\text{rot}} > 25$ d; only 1 of these stars was assigned a value of β (obtained by Landstreet & Mathys 2000). Obliquity angles were derived for all 44 of the stars with $P_{\text{rot}} < 25$ d. We did not identify any clear correlations between β and P_{rot} . We do confirm the findings of Landstreet & Mathys (2000) that β tends to be large for these more rapidly rotating stars (i.e. those with P_{rot} values that are more commonly found amongst mCP stars e.g. Wolff 1975; Bychkov, Bychkova & Madej 2005; Netopil et al. 2017). However, we find that the distribution of β values is consistent with a theoretical distribution of randomly oriented axes. We also did not find any clear correlations between β and absolute stellar age or fractional MS age or between β and B_d . Therefore, we find no evidence that the β values of stars with $P_{\text{rot}} < 25$ d are preferentially oriented as a result of some physical mechanism (e.g. Mestel & Takhar 1972; Moss 1984). We note that this result is consistent with the findings of Wade (1997) who identified both young and evolved mCP stars that exhibit moderate β values ($\sim 30^\circ$).

We were able to constrain the dipole magnetic field strengths for 45/52 of the mCP stars in our sample. The minimum field strength found in our sample when considering the upper error limits of B_d corresponds to 390 G. The fact that we did not find any stars with fields $\lesssim 100$ G is consistent with the notion that there exists a magnetic desert (e.g. Aurière et al. 2007; Lignières et al. 2014). We also derived the critical field strengths of each of the stars, which corresponds to the minimum field strength required for an mCP star's field to remain stable as hypothesized by Aurière et al. (2007). Three stars (HD 29305, HD 56022, and HD 112185)

were found exhibiting upper error limits of $B_d/B_c < 1$; however, no stars were found having $B_d/B_c \ll 1$. These stars may serve as useful targets for constraining B_c , if this critical lower field strength limit does exist.

Although our volume-limited sample does not contain any examples of mCP stars with field strengths well below B_c , several examples of intermediate- and high-mass stars have recently been reported. Fossati et al. (2015) derived a dipole field strength of $60 < B_d < 230$ G for the massive B1 II/III star, β CMa, suggesting that the magnetic desert feature may be limited to the cooler, intermediate mass stars studied by Aurière et al. (2007). On the other hand, Alecian et al. (2016) report a field strength of $B_d = 65 \pm 20$ G for an Ap star with an effective temperature estimated to be 11.4 ± 0.3 kK. This star is the primary component of the spectroscopic binary, HD 5550, which exhibits an orbital period ~ 6.8 d. They find that the magnetic component likely rotates with a period of 6.8 d; no radius or luminosity is reported. Assuming that the star is positioned somewhere on the MS, we obtain a rough estimate of the critical field strength (Eqn. 3) of $130 \lesssim B_c \lesssim 220$ G; therefore, it is likely that $B_d/B_c < 1$. It is possible that the fact that this star is in a binary system with a relatively short period may somehow influence this result, however, considering the > 5 d orbital period, it is unlikely that any tidal interactions are taking place. It is also possible that the order of magnitude estimate of B_c estimated by Aurière et al. (2007) is simply too high or is in need of refinement.

A clear increase in the incidence rate of mCP stars with increasing mass was identified in Paper I (mCP stars account for ≈ 3 per cent of MS stars with $M \approx 1.5 M_\odot$ and ≈ 10 per cent of MS stars with $3.0 < M/M_\odot < 3.8$). The Monte Carlo simulation involving the Zorec & Royer (2012) data did not reveal an increase in B_c with decreasing M , which might have otherwise explained the increased rarity of lower mass mCP stars. We conclude that, regardless of whether B_c exists, this particular property of mCP stars is likely a product of additional factors such as the increase in subsurface convection zone depth with decreasing mass.

In Paper I, we detected the decrease of average surface abundances of certain elements such as Si, Ti, and Fe over stellar age similar to the trends reported by Bailey, Landstreet & Bagnulo (2014) for Bp stars. Here we detect a decrease in B_d over both absolute age and fractional MS age. The rate of B_d decrease is strongest for the highest mass stars in our sample and is found to be in agreement with that reported by Landstreet et al. (2007) based on B_{rms} values. Contrary to the findings reported by Landstreet et al. (2007), we do not detect any change in the surface magnetic flux over time; however, the reported decay rates are in agreement within the adopted uncertainties. We conclude that the lack of detection of surface flux decreases can plausibly be attributed to our smaller sample size and lower age precision.

ACKNOWLEDGMENTS

GAW acknowledges support in the form of a Discovery Grant from the Natural Science and Engineering Research Council (NSERC) of Canada.

REFERENCES

- Abt H. A., 2001, *AJ*, 122, 2008
 Adelman S. J., Dukes, Jr. R. J., Pyper D. M., 1992, *AJ*, 104, 314
 Alecian E. et al., 2014, *A&A*, 567, A28
 Alecian E., Tkachenko A., Neiner C., Folsom C. P., Leroy B., 2016, *A&A*, 589, 1
 Alecian E. et al., 2013, *MNRAS*, 429, 1001
 Aurière M. et al., 2010, *A&A*, 523, A40
 Aurière M. et al., 2007, *A&A*, 475, 1053
 Babcock H. W., 1956, *ApJ*, 124, 489
 Bagnulo S., Innocenti M. L. D., Degl’Innocenti E., 1996, *A&A*, 308, 115
 Bagnulo S., Landi Degl’Innocenti E., Landolfi M., Leroy J. L., 1995, *A&A*, 295, 459
 Bagnulo S., Landolfi M., Degl’Innocenti M., 1999, *A&A*, 343, 865
 Bagnulo S., Landstreet J. D., Mason E., Andretta V., Silaj J., Wade G. A., 2006, *A&A*, 450, 777
 Bailey J. D., Landstreet J. D., Bagnulo S., 2014, *A&A*, 561, A147
 Bayer C., Maitzen H. M., Paunzen E., Rode-Paunzen M., Sperl M., 2000, *A&AS*, 147, 99
 Blazère A., Neiner C., Petit P., 2016, *MNRAS*, 459, L81
 Bohlender D. A., Landstreet J. D., 1990, *ApJ*, 358, L25
 Bohlender D. A., Landstreet J. D., Thompson I. B., 1993, *A&A*, 269, 355
 Borra E. F., Landstreet J. D., 1980, *ApJS*, 42, 421
 Borra E. F., Landstreet J. D., Mestel L., 1982, *ARA&A*, 20, 191
 Braithwaite J., Cantiello M., 2013, *MNRAS*, 428, 2789
 Bychkov V. D., Bychkova L. V., Madej J., 2005, *A&A*, 430, 1143
 Bychkov V. D., Bychkova L. V., Madej J., 2016, *MNRAS*, 455, 2567
 Catalano F. A., Leone F., 1994, *A&AS*, 108, 595
 Catalano F. A., Leone F., Kroll R., 1998, *A&AS*, 129, 463
 Charbonneau P., 2010, *Living Rev. Sol. Phys.*, 7
 Cowling T. G., 1945, *MNRAS*, 105, 166
 Deutsch A. J., 1947, *ApJ*, 105, 503
 Díaz-Cordovés J., Claret A., Gimenez A., 1995, *A&AS*, 110, 329
 Donati J.-F., Catala C., Wade G. A., Gallou G., Delaigue G., Rabou P., 1999, *A&AS*, 134, 149
 Donati J.-F., Semel M., Carter B. D., Rees D. E., Cameron A. C., 1997, *MNRAS*, 291, 658
 Ekström S. et al., 2012, *A&A*, 537, 1
 ESA, ed., 1997, *ESA Special Publication*, Vol. 1200, The HIPPARCOS and TYCHO catalogues. Astrometric and photometric star catalogues derived from the ESA HIPPARCOS Space Astrometry Mission
 Fossati L. et al., 2015, *A&A*, 574, 1
 Georgy C., Ekström S., Granada a., Meynet G., Mowlavi N., Eggenberger P., Maeder a., 2013, *A&A*, 553, 1
 Gokkaya N., 1970, *Astrophys. Space Sci.*, 6, 141
 Grunhut J. H. et al., 2012, *MNRAS*, 419, 1610
 Heck A., Mathys G., Manfroid J., 1987, *A&AS*, 70, 33
 Hill G. M., Bohlender D. A., Landstreet J. D., Wade G. A., Manset N., Bastien P., 1998, *MNRAS*, 297, 236
 Hubrig S., North P., Schöller M., 2007, *Astron. Nachrichten*, 328, 475

- Jasinski M., Muciek M., Woszczyk A., 1981, *Acta Astron.*, 31, 321
- Kochukhov O., Bagnulo S., 2006, *A&A*, 450, 763
- Kochukhov O., Drake N. A., Piskunov N., de la Reza R., 2004, *A&A*, 424, 935
- Kochukhov O., Lundin A., Romanyuk I., Kudryavtsev D., 2011, *ApJ*, 726, 24
- Kochukhov O., Makaganiuk V., Piskunov N., 2010, *A&A*, 524, 1
- Kochukhov O., Rusomarov N., Valenti J. A., Stempels H. C., Snik F., Rodenhuis M., Piskunov N., 2015, *A&A*, 574, 1
- Krtićka J., Mikulášek Z., Lüftinger T., Jagelka M., 2015, *A&A*, 576, 1
- Kurtz D. W., 1982, *MNRAS*, 200, 807
- Kurtz D. W., Sullivan D. J., Martinez P., Tripe P., 1994, *MNRAS*, 270, 674
- Kurtz D. W., van Wyk F., Roberts G., Marang F., Handler G., Medupe R., Kilkeny D., 1997, *MNRAS*, 287, 69
- Landstreet J. D., 1982, *ApJ*, 258, 639
- Landstreet J. D., 1987, *MNRAS*, 225, 437
- Landstreet J. D., 1988, *ApJ*, 326, 967
- Landstreet J. D., Bagnulo S., Andretta V., Fossati L., Mason E., Silaj J., Wade G. A., 2007, *A&A*, 698, 685
- Landstreet J. D., Mathys G., 2000, *A&A*, 359, 213
- Landstreet J. D. et al., 2008, *A&A*, 481, 465
- Lignières F., Petit P., Aurière M., Wade G. A., Böhm T., 2014, in *Proc. IAU Symp. No. 302*, Cambridge University Press, pp. 338–347
- Lignières F., Petit P., Böhm T., Aurière M., 2009, *A&A*, 500, L41
- Maitzen H. M., Albrecht R., Heck A., 1978, *A&A*, 62, 199
- Maitzen H. M., Pressberger R., Paunzen E., 1998, *A&AS*, 128, 573
- Maitzen H. M., Weiss W. W., Wood H. J., 1980, *A&A*, 81, 323
- Makaganiuk V. et al., 2010, *A&A*, 525, 1
- Manfroid J., Mathys G., Heck A., 1985, *A&A*, 144, 251
- Manfroid J., Renson P., 1994, *A&A*, 281, 73
- Mathys G., 1991, *A&AS*, 89, 121
- Mathys G., 1994, *A&AS*, 108, 547
- Mathys G., 2015, in *Phys. Evol. Magn. Relat. Stars*, pp. 3–14
- Mathys G., Hubrig S., 1997, *A&AS*, 124, 475
- Mestel L., Takhar H. S., 1972, *MNRAS*, 156, 419
- Moss D., 1984, *MNRAS*, 209, 607
- Mowlavi N., Eggenberger P., Meynet G., Ekström S., Georgy C., Maeder A., Charbonnel C., Eyer L., 2012, *A&A*, 541, A41
- Musielok B., 1986, *Acta Astron.*, 36, 131
- Musielok B., Lange D., Schoneich W., Hildelrandt G., Zelwanowa E., Hempelmann, G. A. S., 1980, *Astronomische Nachrichten*, 301, 71
- Netopil M., Paunzen E., Hümmerich S., Bernhard K., 2017, *MNRASL*, 468, 2745
- North P., Adelman S. J., 1995, *A&AS*, 111, 41
- North P., Brown D. N., Landstreet J. D., 1992, *A&A*, 258, 389
- Oksala M. E., Wade G. a., Marcolino W. L. F., Grunhut J., Bohlender D., Manset N., Townsend R. H. D., MiMe S. C., 2010, *MNRAS*, 405, L51
- Paunzen E., Maitzen H. M., 2005, *A&A*, 441, 631
- Petit P. et al., 2011, *A&A*, 532, 1
- Petit P. et al., 2010, *A&A*, 523, 1
- Power J., 2007, Master's thesis, Queen's University, Canada
- Press W., 2007, *Numerical Recipes 3rd Edition: The Art of Scientific Computing*. Cambridge University Press
- Preston G. W., 1967, *ApJ*, 150, 547
- Pyper D. M., 1969, *ApJS*, 18, 347
- Pyper D. M., Ryabchikova T., Malanushenko V., Kuschnig R., Plachinda S., Savanov I., 1998, *MNRAS*, 339, 822
- Renson P., Catalano F. A., 2001, *A&A*, 378, 113
- Renson P., Gerbaldi M., Catalano F. A., 1991, *A&AS*, 89, 49
- Renson P., Maitzen H. M., 1978, *A&A*, 65, 299
- Renson P., Manfroid J., 2009, *A&A*, 498, 961
- Ryabchikova T., Piskunov N., Kurucz R. L., Stempels H. C., Heiter U., Pakhomov Y., Barklem P. S., 2015, *Phys. Scr.*, 90
- Schoneich W., Zelvanova E. I., Musielok B., 1988, in *Magnetic Stars*, Glagolevsky Y. V., ed., p. 193
- Shorlin S. L. S., Wade G. A., Donati J.-F., Landstreet J. D., Petit P., Sigut T. A. A., Strasser S., 2002, *A&A*, 392, 637
- Silvester J., Kochukhov O., Rusomarov N., Wade G. A., 2017, *MNRAS*, 471, 962
- Silvester J., Kochukhov O., Wade G. A., 2015, *MNRAS*, 453, 2163
- Skiff B. A., 2014, *VizieR Online Data Catalog*, 1
- Smith M. A., 1971, *AJ*, 76, 896
- Sokolov N. A., 2000, *A&A*, 353, 707
- Spruit H. C., 2002, *A&A*, 381, 923
- Stibbs D. W. N., 1950, *MNRAS*, 110, 395
- Tayler R. J., 1973, *MNRAS*, 161, 365
- van Genderen A. M., 1971, *A&A*, 14, 48
- Wade G. A., 1997, *A&A*, 325, 1063
- Wade G. A., Bagnulo S., Drouin D., Landstreet J. D., Monin D., 2007, *MNRAS*, 376, 1145
- Wade G. A., Donati J.-F., Landstreet J. D., Shorlin S. L. S., 2000, *MNRAS*, 313, 851
- Wade G. A., Hill G. M., Adelman S. J., Manset N., Bastien P., 1998, *A&A*, 335, 973
- Williams M. J., Bureau M., Cappellari M., 2010, *MNRAS*, 409, 1330
- Wolff S. C., 1968, *PASP*, 80, 281
- Wolff S. C., 1969, *ApJ*, 158, 1231
- Wolff S. C., 1975, *ApJ*, 202, 127
- Wraight K. T., Fossati L., Netopil M., Paunzen E., Rode-Paunzen M., Bewsher D., Norton A. J., White G. J., 2012, *MNRAS*, 420, 757
- Ziznovsky J., Mikulasek Z., 1995, *Inf. Bull. Var. Stars*, 1
- Zorec J., Royer F., 2012, *A&A*, 537, A120

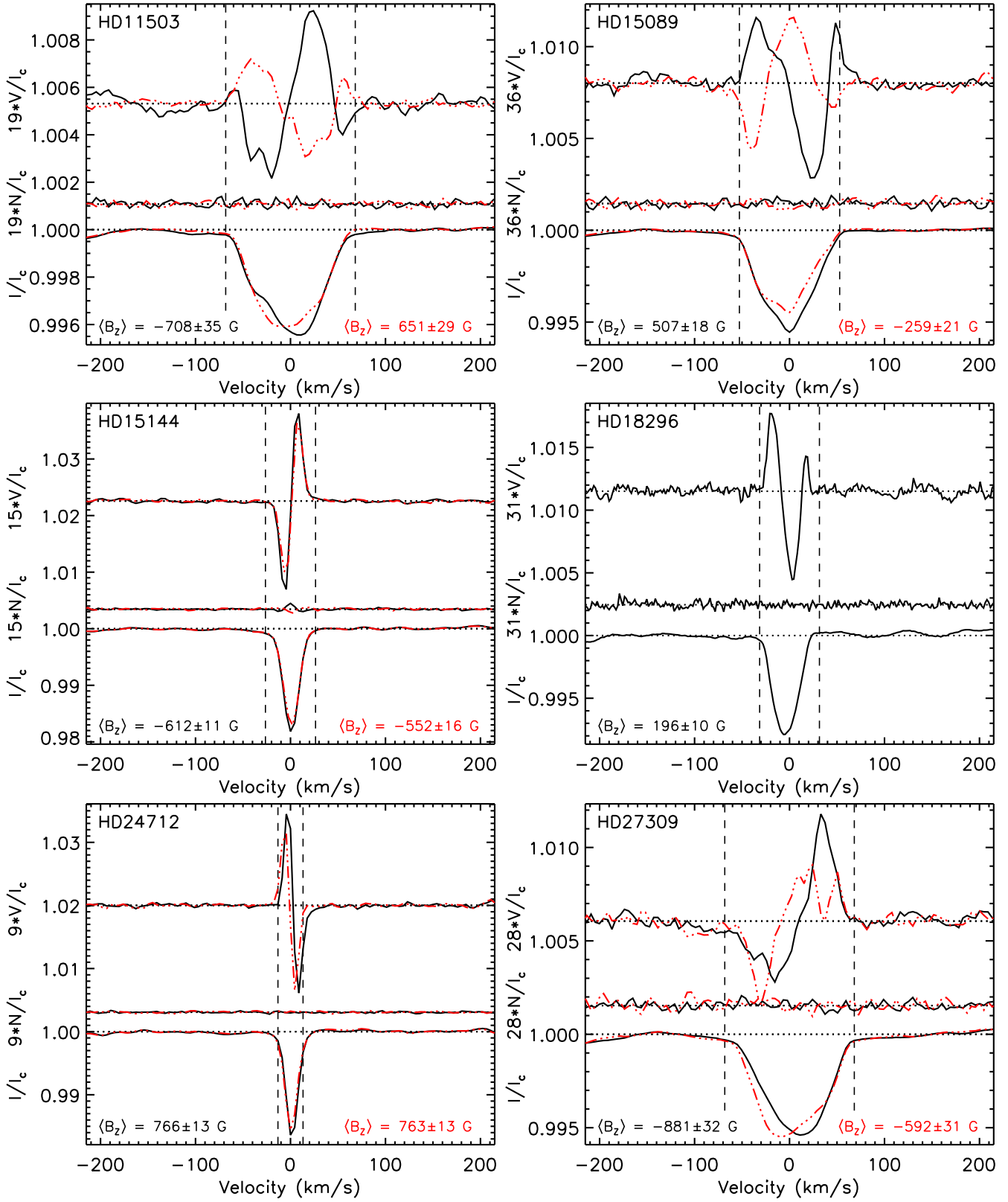


Figure 14. Examples of LSD profiles at one or two rotational phases.

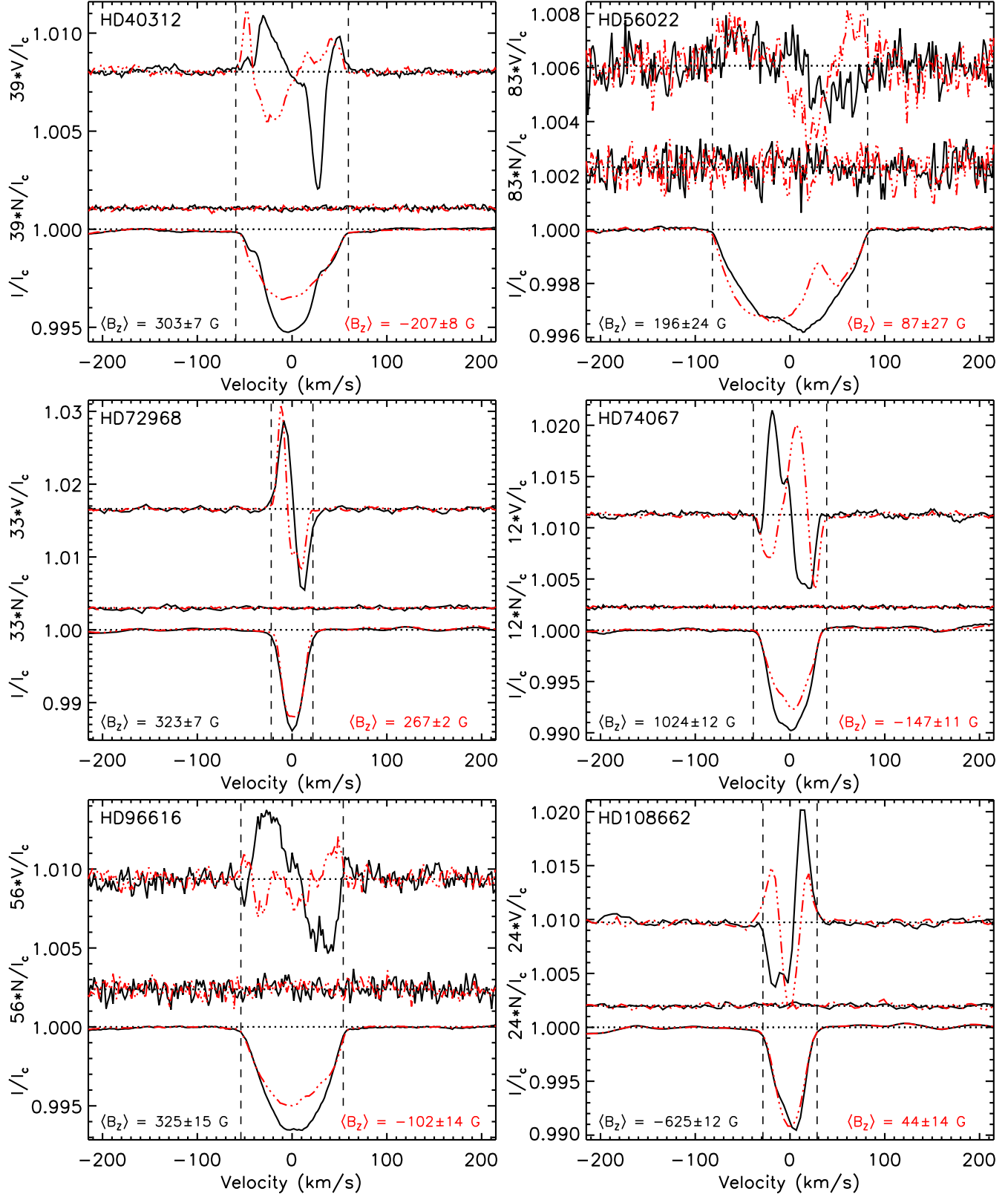


Figure 15. Examples of LSD profiles at one or two rotational phases.

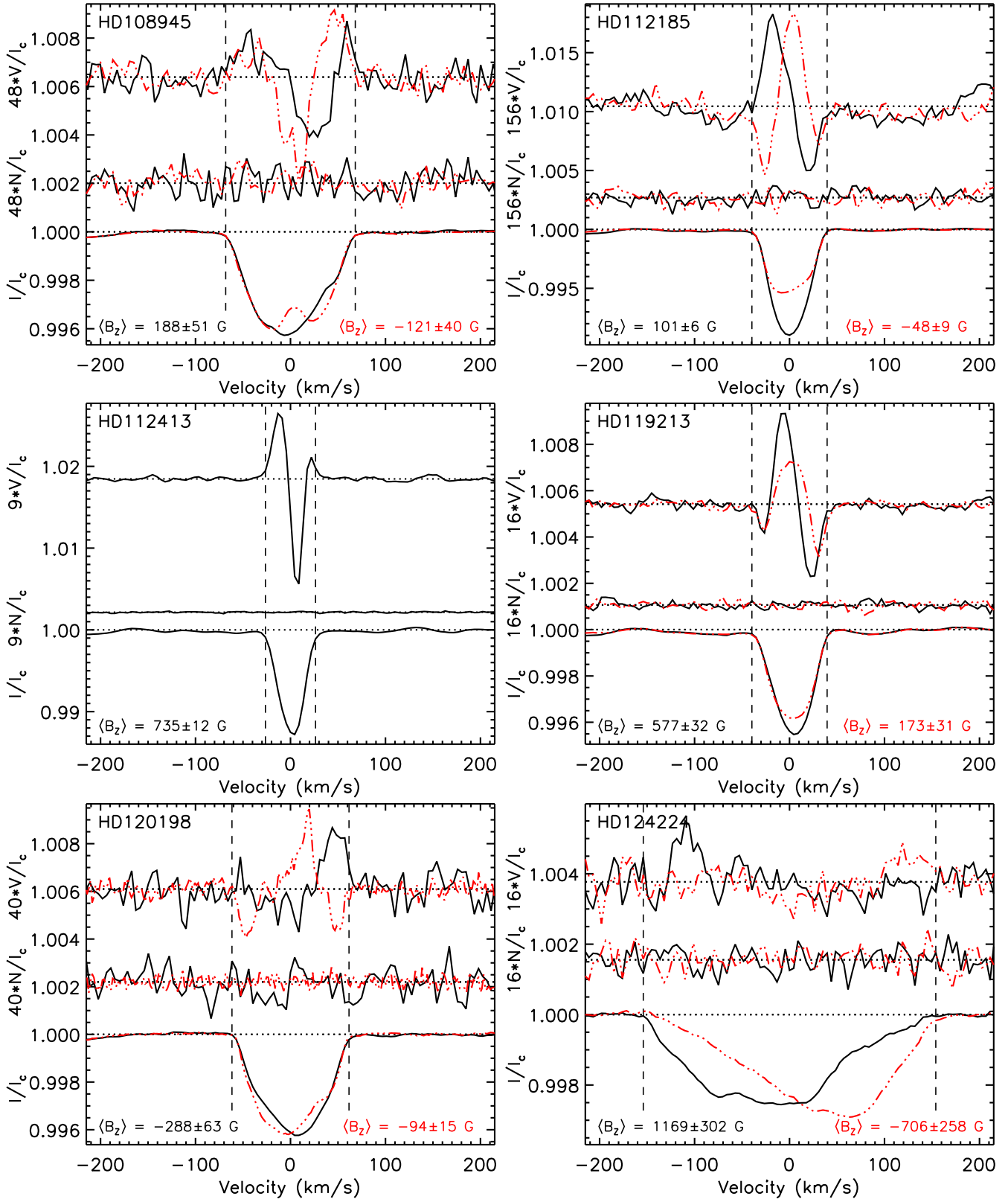


Figure 16. Examples of LSD profiles at one or two rotational phases.

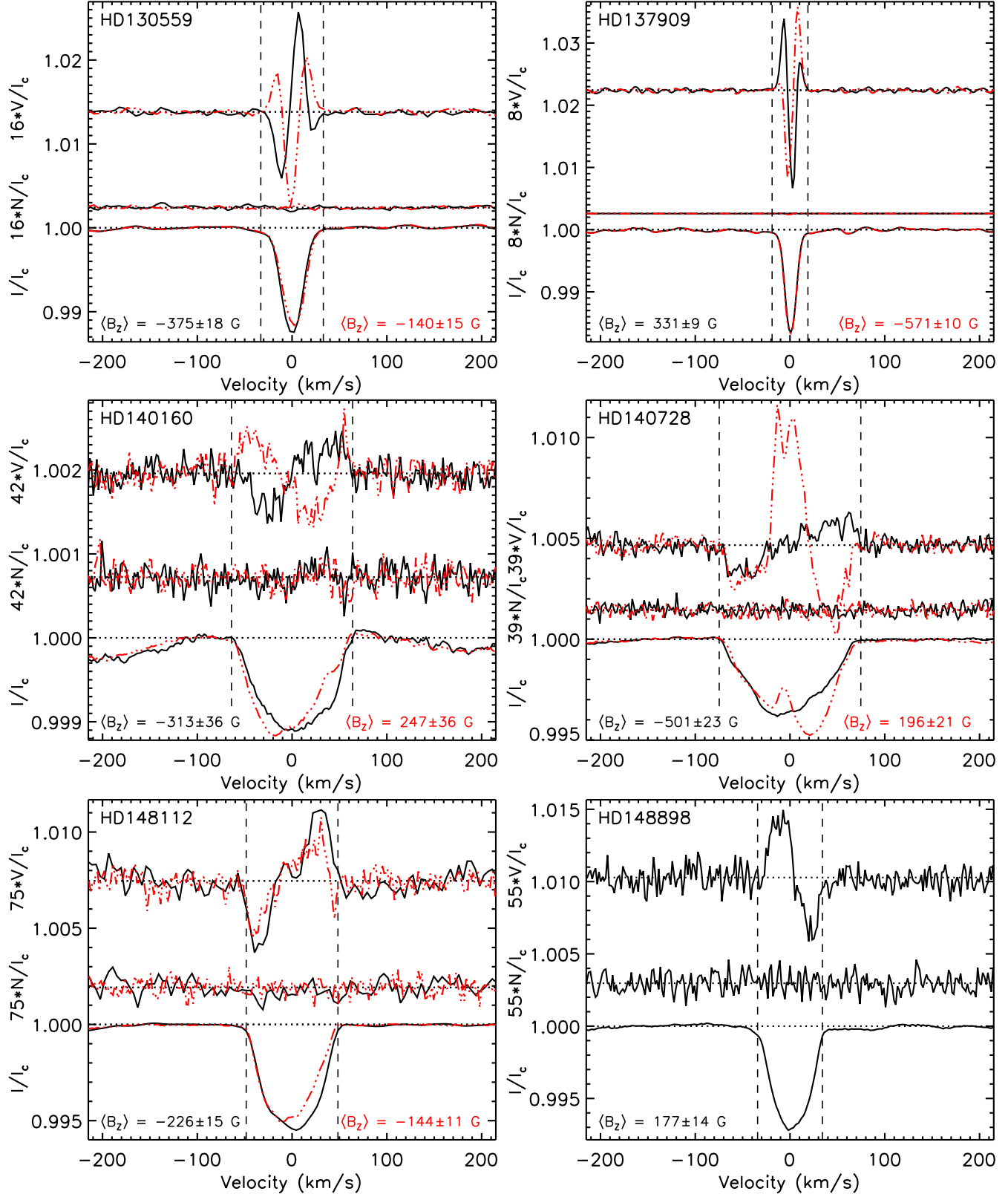


Figure 17. Examples of LSD profiles at one or two rotational phases.

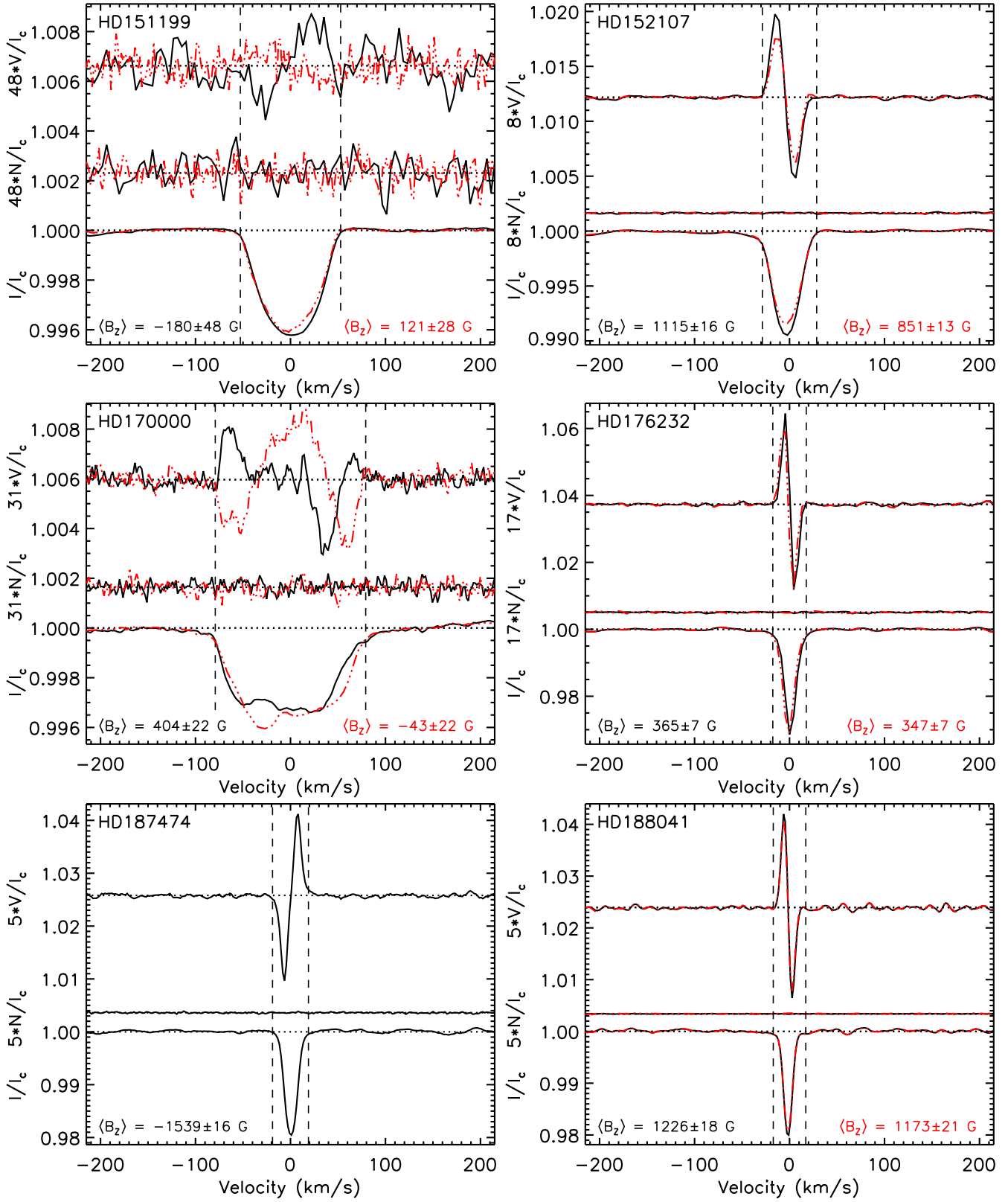


Figure 18. Examples of LSD profiles at one or two rotational phases.

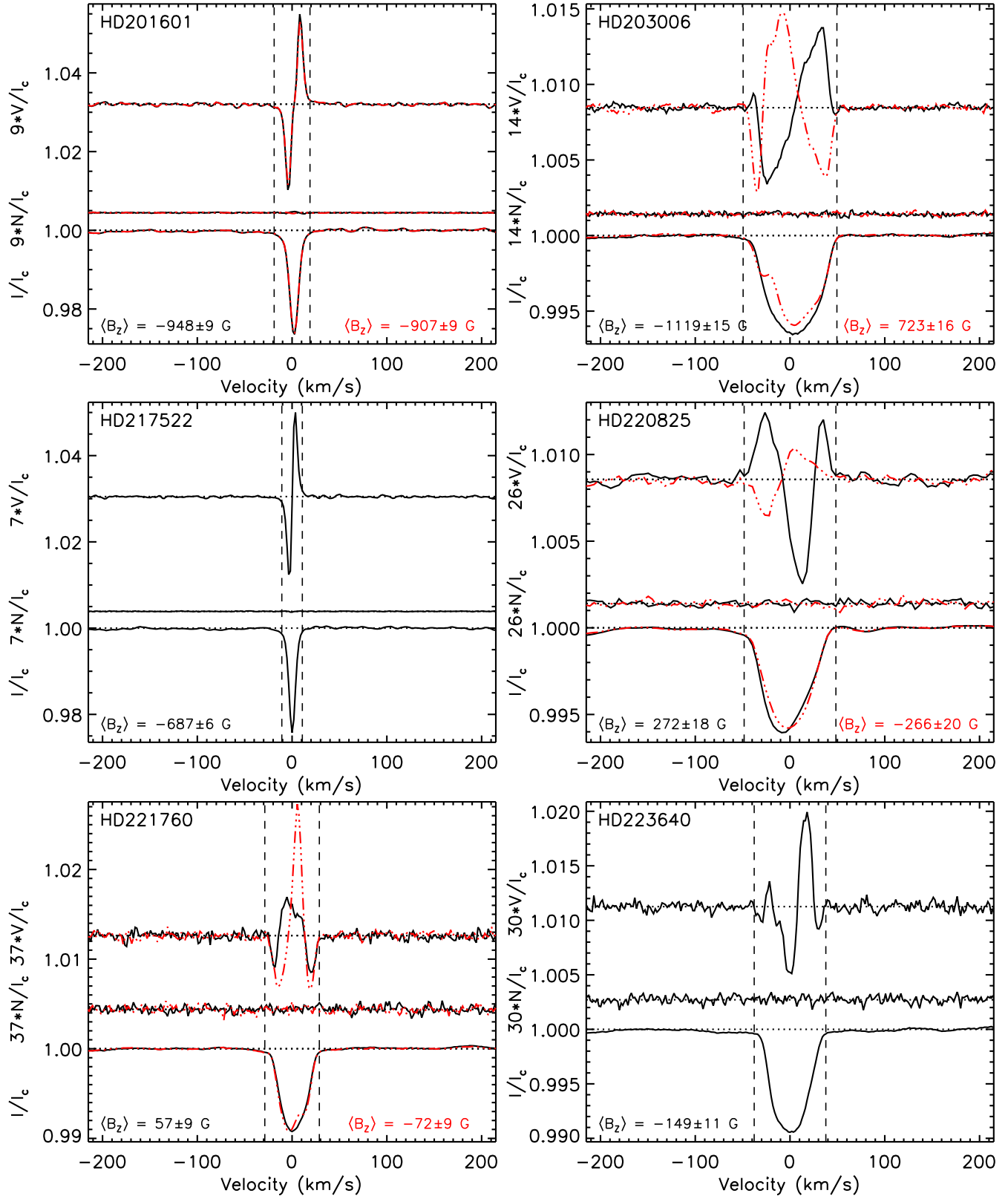


Figure 19. Examples of LSD profiles at one or two rotational phases.

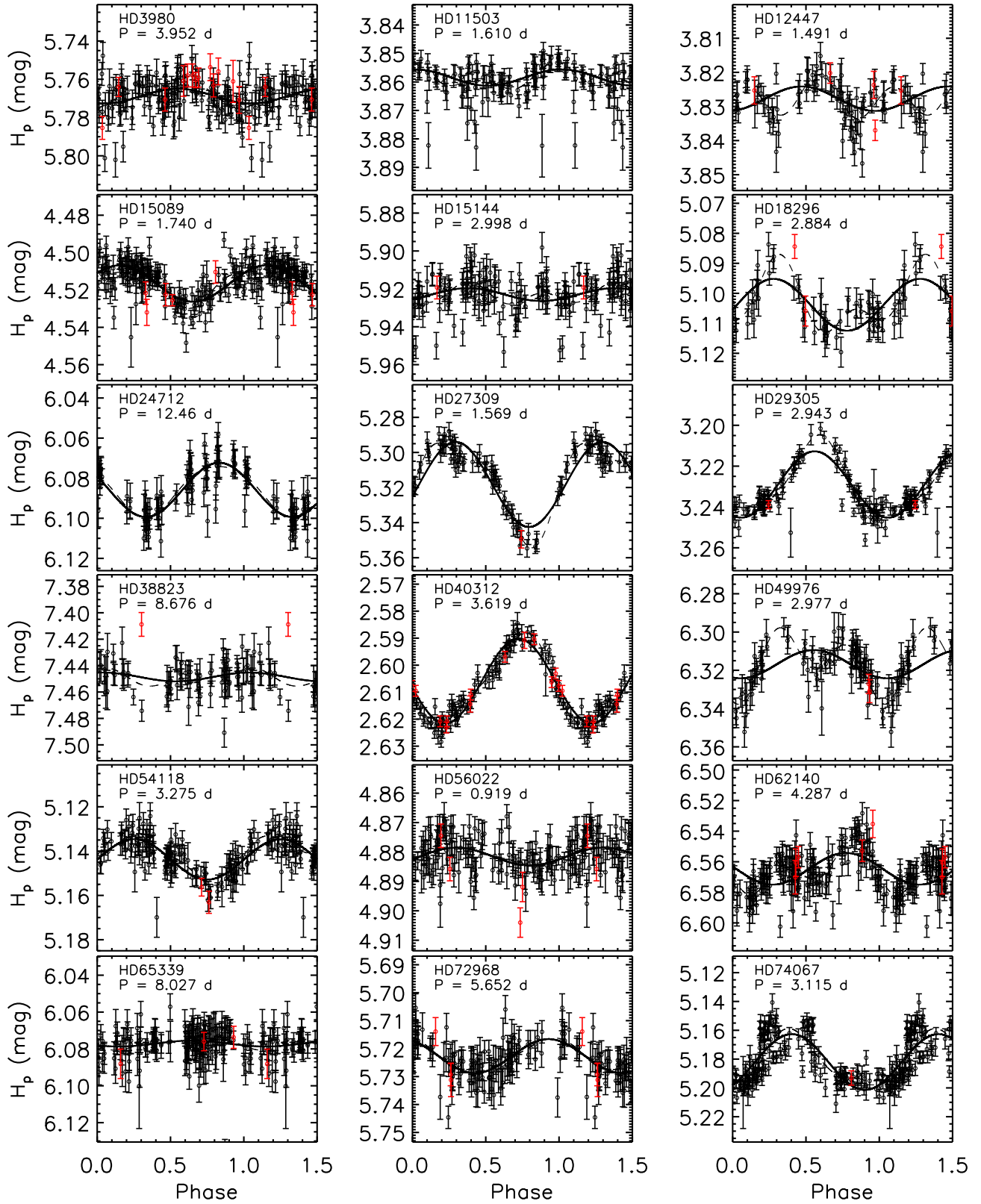


Figure 20. The Hipparcos Epoch Photometry associated with those mCP stars with known P_{rot} . The solid black curves and dashed black curves correspond to the best 1st and 2nd order sinusoidal fits (defined by Eqn. 1). Note that the periods listed in each figure are rounded and do not correspond to the actual P_{rot} precision.

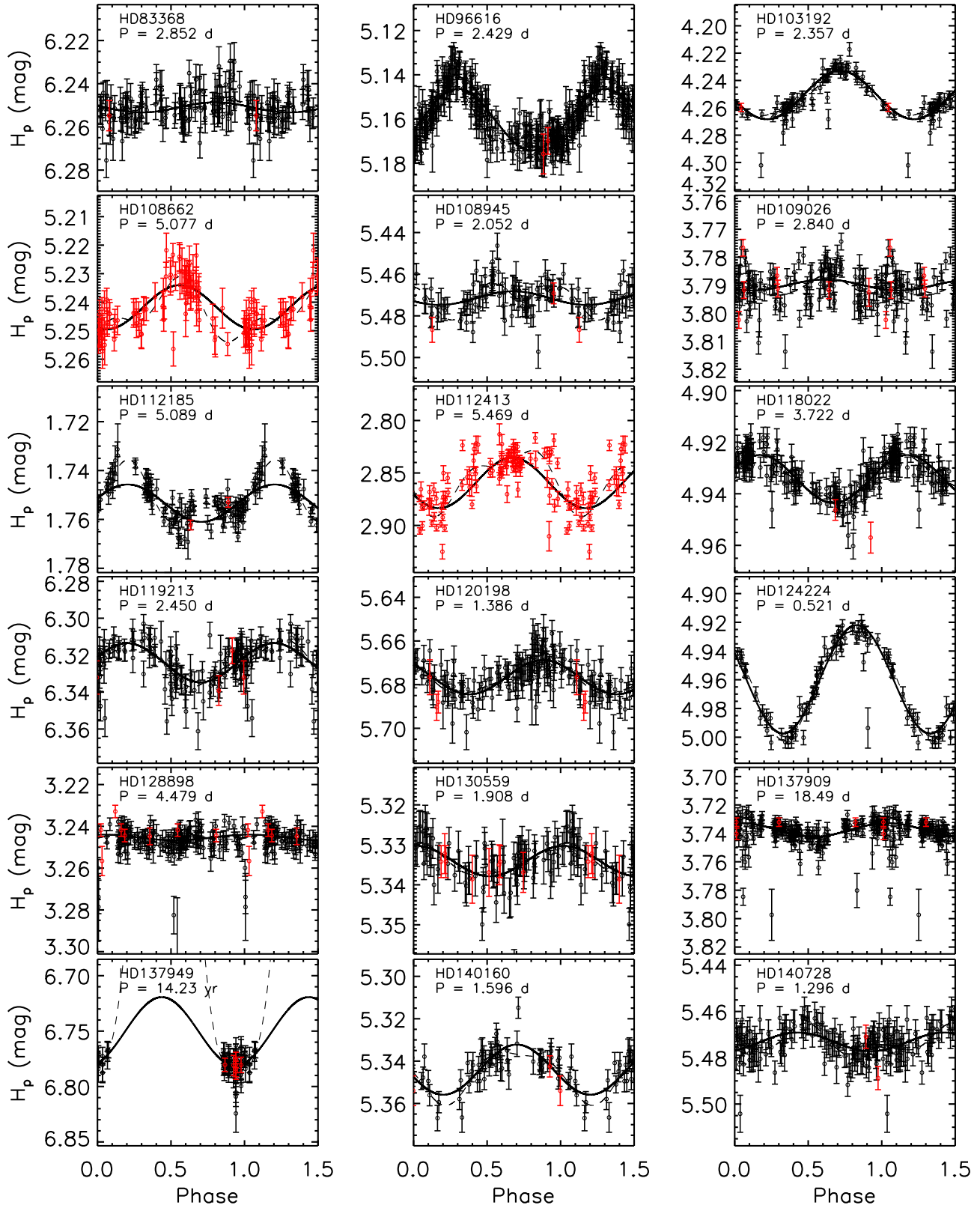


Figure 21. Continued from Fig. 20.

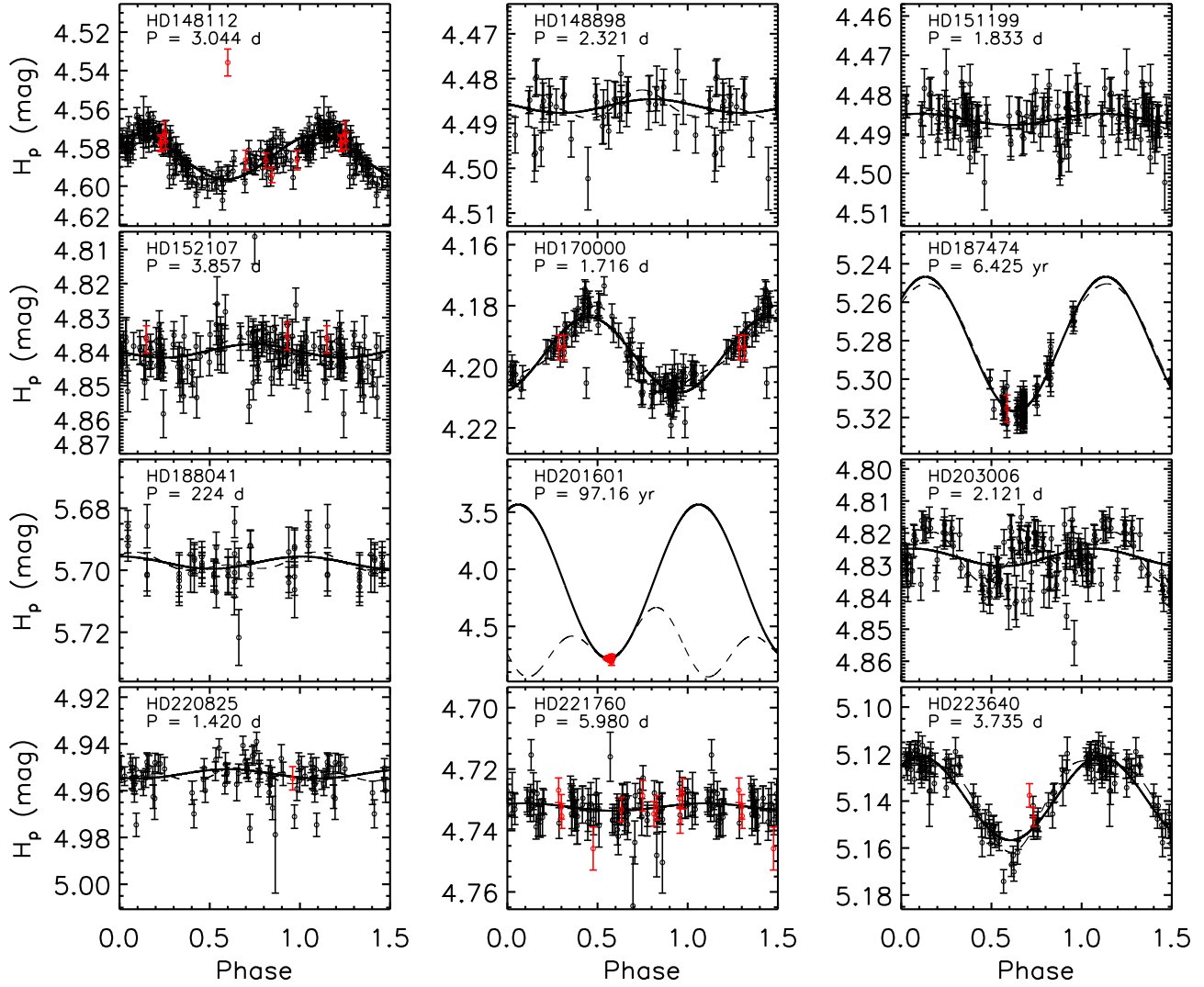


Figure 22. Continued from Fig. 21.

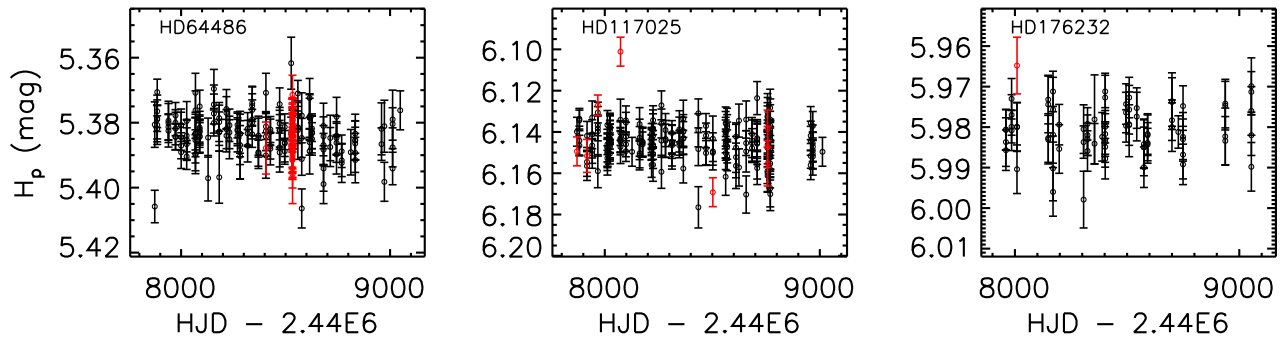

 Figure 23. The Hipparcos Epoch Photometry associated with those stars without known P_{rot} values.

Table 6. Observations of confirmed mCP stars – those stars for which at least one definite detection was obtained based on the criterion proposed by Donati et al. (1997). Columns 1 to 5 contain the HD number, instrument used to obtain the observation (ESP = ESPaDOnS, MUS = MuSiCoS, and NAR = NARVAL), HJD, rotational phase, and the derived $\langle B_z \rangle$ value and its associated uncertainty.

HD	Inst.	HJD	Phase	$\langle B_z \rangle$ (kG)	HD	Inst.	HJD	Phase	$\langle B_z \rangle$ (kG)
15089	MUS	3040.343	0.259	223 ± 93		MUS	3883.398	0.308	151 ± 68
	MUS	3586.543	0.077	450 ± 23		MUS	3891.405	0.489	526 ± 93
	MUS	3589.652	0.864	506 ± 18		MUS	3894.399	0.799	-188 ± 73
	MUS	3590.561	0.386	-258 ± 20		ESP	7264.753	0.204	-177 ± 24
	MUS	3591.597	0.981	509 ± 19		ESP	7284.802	0.679	196 ± 21
	MUS	3594.551	0.678	-166 ± 24		ESP	7285.774	0.430	463 ± 40
	MUS	3607.557	0.150	441 ± 32		ESP	7287.736	0.944	-500 ± 23
	MUS	3616.513	0.296	11 ± 24		ESP	7289.704	0.463	464 ± 24
15144	MUS	2253.385	0.716	-568 ± 13	148112	MUS	2856.386	0.347	-168 ± 20
	MUS	2254.408	0.057	-619 ± 12		MUS	3586.413	0.159	-236 ± 25
	MUS	3410.324	0.620	-567 ± 18		MUS	3588.399	0.812	-167 ± 14
	MUS	3613.503	0.392	-551 ± 15		MUS	3589.394	0.139	-233 ± 33
	MUS	3615.559	0.078	-612 ± 10		MUS	3598.384	0.092	-225 ± 14
	MUS	3617.570	0.749	-586 ± 11		MUS	3618.364	0.655	-170 ± 18
18296	ESP	7556.127	0.190	91 ± 19		ESP	7523.032	0.330	-144 ± 10
	ESP	7561.124	0.923	169 ± 19		ESP	7560.973	0.794	-218 ± 15
	ESP	7610.142	0.918	195.7 ± 9.7		ESP	7563.737	0.702	-170 ± 10
24712	MUS	857.333	0.180	765 ± 13	148898	ESP	7264.745	0.370	-30 ± 18
	MUS	1924.360	0.830	763 ± 12		ESP	7285.720	0.409	-94 ± 20
56022	MUS	3247.675	0.052	1033 ± 17		ESP	7287.729	0.275	176 ± 13
	ESP	7325.149	0.210	139 ± 32		ESP	7297.700	0.571	-117.7 ± 9.8
	ESP	7438.845	0.941	195 ± 24		MUS	3864.579	0.701	-26 ± 56
	ESP	7443.892	0.434	-81 ± 36		MUS	3866.496	0.746	18 ± 57
72968	ESP	7447.848	0.739	86 ± 26		MUS	3874.543	0.136	-179 ± 47
	MUS	3748.583	0.774	346.4 ± 8.4		MUS	3880.530	0.402	49 ± 48
	MUS	3749.549	0.945	343.0 ± 7.3		MUS	3883.512	0.029	-246 ± 50
	MUS	3755.429	0.985	307 ± 16		MUS	3885.510	0.119	-225 ± 49
	MUS	3756.527	0.179	323.5 ± 7.0		MUS	3890.483	0.831	-244 ± 50
74067	ESP	7416.994	0.763	334.1 ± 5.2	152107	MUS	3893.479	0.466	80 ± 74
	ESP	7498.720	0.221	335.2 ± 3.8		ESP	7264.762	0.511	120 ± 27
	ESP	7500.781	0.586	266.8 ± 2.5		MUS	3601.389	0.107	1278 ± 16
	ESP	7330.146	0.046	1024 ± 11		MUS	3617.372	0.251	912 ± 12
	ESP	7331.099	0.352	-147 ± 10		MUS	3747.719	0.041	1349 ± 19
	ESP	7348.156	0.828	748 ± 38		MUS	3758.748	0.900	1194 ± 17
	ESP	7415.993	0.605	-303 ± 12		MUS	3759.711	0.150	1164 ± 16
	ESP	7440.875	0.592	-370 ± 34		MUS	3760.763	0.423	636 ± 19
	ESP	7445.857	0.192	562 ± 26		MUS	3761.760	0.681	850 ± 13
	ESP	7446.838	0.506	-480 ± 28		MUS	3774.753	0.049	1365 ± 16
96616	ESP	7358.169	0.668	-58 ± 15	170000	MUS	3866.586	0.856	1114 ± 15
	ESP	7441.990	0.172	213 ± 16		MUS	3872.548	0.401	683 ± 14
	ESP	7444.970	0.399	-153 ± 22		MUS	3601.424	0.435	-186 ± 56
	ESP	7447.937	0.620	-101 ± 13		MUS	3607.362	0.894	560 ± 130
	ESP	7448.964	0.043	325 ± 14		MUS	3608.371	0.482	-206 ± 86
108662	MUS	1612.541	0.893	-647 ± 11		MUS	3615.369	0.559	-179 ± 59
	MUS	3747.645	0.408	44 ± 13		MUS	3872.511	0.366	-250 ± 110
	MUS	3750.726	0.015	-625 ± 11		MUS	3874.576	0.569	-98 ± 82
	MUS	3756.707	0.193	-645 ± 12		MUS	3891.554	0.460	-176 ± 68
	MUS	3757.581	0.365	-200 ± 14		NAR	7621.404	0.412	-236 ± 23

continued on next page

continued from previous page

HD	Inst.	HJD	Phase	$\langle B_z \rangle$ (kG)	HD	Inst.	HJD	Phase	$\langle B_z \rangle$ (kG)
108945	MUS	3758.588	0.564	262 ± 17	176232	NAR	7622.371	0.975	403 ± 22
	MUS	3759.749	0.792	-633 ± 13		NAR	7623.420	0.587	-195 ± 30
	MUS	3864.378	0.399	-4 ± 15		NAR	7624.424	0.171	436 ± 22
	MUS	3891.370	0.715	-398 ± 17		NAR	7625.417	0.750	163 ± 25
	MUS	1612.576	0.328	111 ± 42		NAR	7630.451	0.682	-10 ± 29
	MUS	3405.675	0.217	-7 ± 49		NAR	7631.520	0.305	-42 ± 21
	MUS	3410.674	0.653	18 ± 51		NAR	7634.390	0.978	431 ± 23
	MUS	3752.664	0.327	187 ± 51		NAR	7635.370	0.548	-148 ± 27
	MUS	3755.575	0.745	-22 ± 94		NAR	7638.400	0.314	-80 ± 22
112185	MUS	3756.589	0.239	-120 ± 39	187474	NAR	7639.406	0.900	369 ± 24
	MUS	3748.683	0.160	84 ± 10		NAR	7640.393	0.475	-288 ± 21
	MUS	3749.648	0.349	-47.9 ± 8.6		NAR	7644.313	0.758	147 ± 27
112413	MUS	3752.737	0.956	101.1 ± 5.9	188041	NAR	7734.235	0.145	497 ± 31
	MUS	3202.378	0.438	734 ± 11		NAR	7735.233	0.727	79 ± 29
119213	MUS	3406.516	0.105	641 ± 50	201601	NAR	7736.233	0.309	-68 ± 21
	MUS	3409.673	0.394	68 ± 53		NAR	7737.234	0.892	393 ± 24
120198	MUS	3411.615	0.186	517 ± 44	203006	NAR	7801.720	0.461	-299 ± 24
	MUS	3412.613	0.594	169 ± 55		NAR	7802.707	0.036	459 ± 22
	MUS	3746.637	0.935	647 ± 40		NAR	7803.706	0.618	-77 ± 26
	MUS	3749.679	0.176	577 ± 31		NAR	7804.696	0.195	371 ± 25
	MUS	3752.704	0.411	79 ± 36		MUS	2827.591		396.4 ± 8.9
	MUS	3757.619	0.417	15 ± 41		MUS	2835.485		383 ± 11
	MUS	3758.625	0.828	453 ± 55		MUS	2854.413		401 ± 52
	MUS	3760.664	0.660	299 ± 51		MUS	3217.404		363 ± 42
	MUS	3761.640	0.059	373 ± 78		MUS	3585.441		371.7 ± 8.6
	MUS	3762.668	0.478	13 ± 91		MUS	3589.436		369.0 ± 8.6
	MUS	3767.676	0.522	149 ± 40		MUS	3595.388		365.3 ± 6.8
	MUS	3768.625	0.910	580 ± 310		MUS	3881.556		344 ± 20
	MUS	3769.647	0.327	173 ± 31		MUS	3887.492		349.2 ± 8.3
	MUS	3773.574	0.930	643 ± 38		MUS	3892.524		346.6 ± 7.4
	ESP	7522.776	0.270	430 ± 81		MUS	3893.521		339.8 ± 8.7
	MUS	1601.676	0.529	-287 ± 62		ESP	7239.990		244.9 ± 4.7
	ESP	7522.837	0.391	-93 ± 15		ESP	7554.103	0.126	-1539 ± 16
124224	MUS	3746.675	0.213	580 ± 220		MUS	2838.532	0.103	1294 ± 24
	MUS	3756.751	0.565	-710 ± 260		MUS	2848.513	0.147	1266 ± 22
130559	MUS	3757.657	0.305	-360 ± 220		MUS	2857.421	0.187	1231 ± 23
	MUS	3758.662	0.234	280 ± 250		MUS	3210.444	0.763	1130 ± 25
	MUS	3759.635	0.104	1170 ± 300		MUS	3213.481	0.776	1145 ± 24
	MUS	3406.743	0.544	-64 ± 30		ESP	7239.981	0.752	1173 ± 21
	MUS	3411.649	0.115	-432 ± 20		ESP	7263.818	0.858	1318 ± 22
	MUS	3746.712	0.727	-276 ± 16		ESP	7564.127	0.199	1226 ± 18
	MUS	3755.725	0.451	-81 ± 21		ESP	7239.998	0.135	-948.0 ± 9.0
	MUS	3757.693	0.482	-64 ± 16		ESP	7564.132	0.144	-907.1 ± 8.7
	MUS	3759.671	0.519	-32 ± 18		ESP	7236.944	0.205	-345 ± 25
	MUS	3760.708	0.062	-416 ± 20		ESP	7239.989	0.641	723 ± 15
140160	MUS	3768.712	0.257	-295 ± 16	217522	ESP	7261.783	0.917	-1019 ± 16
	MUS	3770.716	0.308	-213 ± 20		ESP	7264.821	0.350	720 ± 21
	MUS	3774.688	0.390	-139 ± 14		ESP	7284.829	0.784	-241 ± 21
	MUS	3880.431	0.811	-374 ± 18		ESP	7296.836	0.446	987 ± 21
	MUS	3893.383	0.599	-99 ± 19		ESP	7327.765	0.030	-1119 ± 14
	MUS	1606.632	0.760	-200 ± 160		ESP	7287.834		-686.7 ± 5.6
	MUS	3864.501	0.581	620 ± 200		MUS	3585.630	0.396	-196 ± 20
	MUS	3889.556	0.280	15 ± 88		MUS	3588.558	0.458	-265 ± 19
	ESP	7239.821	0.615	278 ± 38		MUS	3589.625	0.209	175 ± 18

continued on next page

continued from previous page

HD	Inst.	HJD	Phase	$\langle B_z \rangle$ (kG)	HD	Inst.	HJD	Phase	$\langle B_z \rangle$ (kG)
140728	ESP	7261.774	0.371	246 ± 35	221760	MUS	3590.531	0.847	272 ± 17
	ESP	7265.754	0.865	-216 ± 45		MUS	3598.585	0.517	-286 ± 21
	ESP	7284.726	0.753	-26 ± 40		MUS	3607.515	0.805	232 ± 33
	ESP	7326.684	0.045	-312 ± 35		ESP	7262.006	0.694	-17 ± 10
	ESP	7407.173	0.481	230 ± 46	223640	ESP	7326.820	0.532	-71.8 ± 8.7
	MUS	3864.537	0.750	-54 ± 75		ESP	7328.763	0.857	57.3 ± 9.5
	MUS	3866.424	0.207	-165 ± 71		ESP	7330.817	0.201	32.9 ± 8.8
	MUS	3872.445	0.855	-460 ± 110		ESP	7611.144	0.509	-148 ± 11